INNOVATIVE NANOMATERIALS FOR EFFICIENT CO_2 PHOTOCATALYTIC CONVERSION TO FUELS

A Dissertation

by

HUILEI ZHAO

Submitted to the Office of Graduate and Professional Studies of
Texas A&M University
in partial fulfillment of the requirements for the degree of

DOCTOR OF PHILOSOPHY

Chair of Committee,	Ying Li
Committee Members,	M. M. Faruque Hasan
	Partha Mukherjee
	Choongho Yu
Head of Department,	Andreas A. Polycarpou

August 2017

Major Subject: Mechanical Engineering

ABSTRACT

Photocatalytic reduction of CO_2 with water by photocatalysts such as TiO_2 to produce solar fuels is an attractive approach to alleviate the environmental influences of greenhouse gasses and in the meantime produce valuable solar fuels. However, TiO_2 has several limitations for CO_2 photoreduction. First, TiO_2 has a large band gap, leading to the low solar energy usage efficiency. Second, the fast charge recombination rate in TiO_2 causes the low photocatalytic performance. Third, relatively insufficient CO_2 adsorption capability results in the low production rate of solar fuels. This work addressed the above limitations by designing innovative TiO_2 based photocatalysts for CO_2 photoreduction with H_2O from four different aspects: (1) crystal structures, (2) CO_2 gas adsorption capability, (3) exposed facets and (4) defect property.

First, this study demonstrated the high performance of mixed anatase/brookite phase TiO_2 for CO_2 photoreduction with H_2O. Single-phase anatase and brookite, and mixed-phase anatase/brookite TiO_2 nanomaterials were synthesized and evaluated for CO_2 photoreduction in the presence of water vapor for the production of solar fuels (CO and CH_4). The results showed that bicrystalline anatase/brookite was more active than single-phase anatase, brookite, and P25. The bicrystalline mixture with a composition of 75% anatase and 25% brookite showed the highest photocatalytic activity, likely due to the enhanced interfacial charge transfer between anatase and brookite nanocrystals.

Second, this study showed improved CO_2 adsorption and conversion by combing CO_2 adsorbents LDHs materials with photocatalyst TiO_2. A novel material of crystallized

titanium-embedded magnesium-aluminum layered double hydroxides (MgAlTi-LDHs) is developed and tested for CO_2 photoreduction with water. Three different materials synthesis methods were explored: (1) coprecipitation, (2) coprecipitation + hydrothermal, and (3) coprecipitation + calcination + reconstruction. The material hydrothermally treated at 150 to 200 °C demonstrated the highest CO production due to a well-balanced TiO_2 crystallinity and specific surface area.

Third, high-performance TiO_2 photocatalysts by combining the effect of oxygen deficiency and exposing facets were synthesized. And atomic layer deposition (ALD) technique was applied to deposit Al_2O_3 thin film on the surface of TiO_2 with thickness of Al_2O_3 controlled by the number of ALD cycles. All the synthesized photocatalysts (ANR, ReANR, and Al_2O_3 coated ReANR) were tested for CO_2 photocatalytic reduction with water. Compared with ANR, ReANR had more than 50% higher CO production and more than ten times higher CH_4 production due to the oxygen vacancies that possibly enhanced CO_2 adsorption and activation. By applying less than 5 cycles of ALD, the Al_2O_3 coated ReANR had enhanced overall production of CO and CH_4 than uncoated ReANR, with 2 cycles being the optimum. Whereas, both CO and CH_4 production decreased with increasing number of ALD cycles when more than 5 cycles were applied. Photoluminescence (PL) analysis showed both 2 and 200 cycles of Al_2O_3 ALD coating on the ReANR were able to reduce the charge carrier recombination rate, likely because of the passivation of surface states. On the other hand, a relatively thick layer (e.g. 200 cycles) of Al_2O_3 may act as an insulation layer to prohibit electron migration to the catalyst surface.

DEDICATION

To my dearest father, without whose support and understanding, I would not be able to complete my Ph.D. study. I am sorry that I could not be there for his last moment, but I believe he knows how much I love him and how much I wanted to be with him. I also believe he would be very happy if he were able to see my completed dissertation.

I also want to dedicate this dissertation to my strong mother, and my younger sister, who took care of my farther meticulously without any complain. No one can imagine how much pressure they suffered. I have to apologize that I did not contribute much during that dark period of our family.

Finally, I would like to dedicate this work to my dear husband, Xiaoru Guo, the love of my life, who is also a Ph.D. candidate, at University of Wisconsin-Milwaukee. Thanks for his support, and all the suggestions and help he has given for my research since 2013. The distance between Texas and Wisconsin is never far enough to impair our love.

ACKNOWLEDGEMENTS

I would like to thank my committee chair, Dr. Ying Li. Thank you for being my adviser for 6 years, and giving me enormous valuable suggestions about course work and research. Thank you for the time and effort he spent.

I would also like to thank my committee members, Dr. M. M. Faruque Hasan, Dr. Partha Mukherjee, and Dr. Choongho Yu, for their guidance and support throughout this research.

Thanks also go to my colleagues at University of Wisconsin-Milwaukee, Dr. Cunyu Zhao, Dr. Lianjun Liu, Dr. Qianyi Zhang, and Jianye Xu, who gave me lots of help on material synthesis and characterization. Special thanks go to Dr. Cunyu Zhao, and Dr. Lianjun Liu for guiding me to the right track at the beginning of my Ph.D. journey and giving me inspirations and supports for my research.

I would also like to thank my colleagues at Texas A&M University, Dr. Fuping Pan, Dr. Guiying Rao, Jiatang Chen, Wei Deng, Jacob Trzaskos, and Tyler Scott for making my time at Texas A&M University a great experience.

CONTRIBUTORS AND FUNDING SOURCES

This work was supervised by a dissertation committee consisting of Professor Ying Li (advisor), Professor Partha Mukherjee and Professor Choongho Yu of the Department of Mechanical Engineering and Professor M. M. Faruque Hasan of Chemical Engineering Department.

All work for the dissertation was completed independently by the student.

This work was supported by U.S National Science Foundation (NSF) CBET-1067233, CBET-1067340, CAREER Award CBET-1254709 and CBET-1538404.

NOMENCLATURE

ALD	Atomic Layer Deposition
ANP	Anatase Nanoparticles
ANR	Anatase Nanorods
BET	Brunauer, Emmett and Teller Method
BJH	Barrett-Joyner-Halenda Method
CB	Conduction Band
DFT	Density Functional Theory
DI	Deionized
DRIFTS	Diffuse Reflectance Infrared Fourier Transform Spectroscopy
EDS	Energy Dispersion X-ray Spectroscopy
FID	Flame Ionized Detector
FTIR	Fourier Transform Infrared Spectroscopy
GC	Gas Chromatography
HRTEM	High-Resolution Transmission Electron Microscopy
IR	Infrared
LDHs	Layered Double Hydroxides
LDOs	Layered Double Oxides
MMO	Mixed Metal Oxide
PL	Photoluminescence
Re-ANR	Reduced Anatase nanorods

Re-ANP	Reduced Anatase Nanoparticles
SEM	Scanning Electron Microscopy
TCD	Thermal Conductivity Detector
TEM	Transmission Electron Microscopy
TGA	Thermogravimetric Analysis
TiO_2	A: Anatase B: Brookite R: Rutile
UV	Ultraviolet
UVvis	Ultraviolet-visible
VB	Valence Band
XPS	X-ray Photoelectron Spectroscopy
XRD	X-ray Diffraction

TABLE OF CONTENTS

Page

LIST OF FIGURES

Page

LIST OF TABLES

Page

1. INTRODUCTION AND LITERATURE REVIEW[1]

1.1 Introduction

Burning fossil fuel as the energy supply for human activities results in massive amounts of CO_2 emissions to the atmosphere, which is the primary cause of the global warming effects. Meanwhile, due to the relatively limited conventional energy source i.e. fossil fuel, in contrast with the enormous energy need by the human society, the development of renewables, e.g. solar energy application technique is essential. The conversion of solar energy into fuels using CO_2 as the feedstock by photocatalysts offers significant promise in the development of a sustainable energy technology.[1-5]

CO_2 photoreduction with H_2O can be understood in two steps. First, CO_2 and H_2O molecules are adsorbed onto catalyst surface, and this process requires high surface area and low physical and chemical energy barriers. Secondly, the photocatalytic process induces excitons from photons and initiates the photoreduction process. The second step in detail can be described in the following sub-steps (shown in **Figure 1**): (1) photo-illumination on the surface of photocatalyst induces the generation of charge carriers, i.e. electron-hole ($e^- - h^+$) pairs; (2) the excited electrons in the conduction band (CB) of photocatalyst could migrate to the surface and reduce CO_2 to solar fuels (e.g., CO, CH_4, CH_3OH, HCOOH), and (3) the holes left in the valence band (VB) of the photocatalyst could oxidize H_2O into oxygen.[6] Possible reactions involved in CO_2 photoreduction with

[1] Part of this chapter is reprinted with permission from "A review on the effects of TiO_2 surface point defects on CO_2 photoreduction with H_2O" by Huilei Zhao, Fuping Pan and Ying Li, 2016. *Journal of Materiomics*, 3, 17-32, Copyright [2016] by Elsevier B.V.

H_2O on TiO_2 and thermodynamic reduction/oxidation potentials of various compounds are listed in **Table 1**.

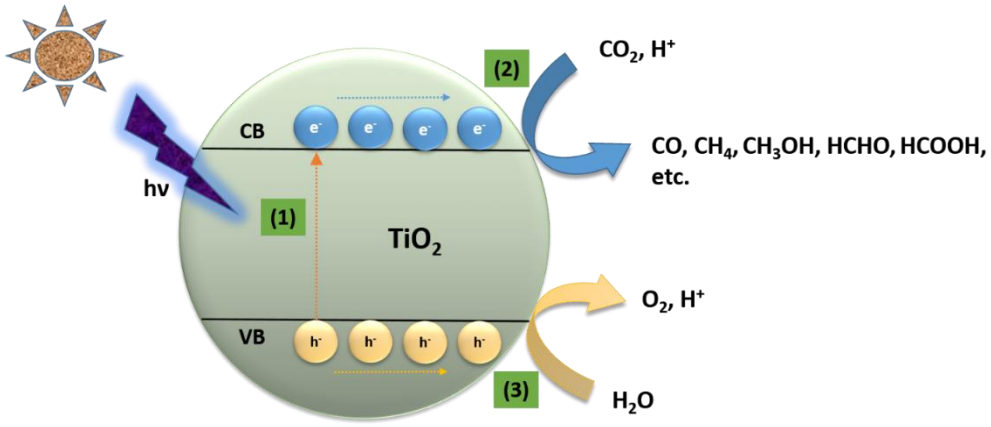

Figure 1 Schematic illustration of the photocatalytic process in the CO_2 photoreduction with H_2O

In the process of CO_2 photoreduction with H_2O, photocatalysts played a significant role to initiate the reaction and convert photo energy to chemical energy. The appropriate photocatalysts for the artificial photosynthesis need to be cost-effective, earth-abundant, non-toxic, and resistant to photo-corrosion. Besides, the electronic properties of the photocatalyst need to meet the following requirement: (1) the conduction band of the photocatalyst should be more negative than the reduction potential of CO_2; and (2) the valence band should be more positive than the oxidation potential of H_2O. Due to the thermodynamically stable nature of the CO_2 molecule and energetically unfavorable nature of photoreduction processes, advanced photocatalysts design are required to facilitate the CO_2 photoreduction and boost the solar energy conversion efficiency.

Table 1 Possible reactions involved in photocatalytic reduction of CO_2 with H_2O on TiO_2 and thermodynamic reduction/oxidation potentials of various compounds

Reaction Equation	Redox pairs	Redox potential[9,11-13] (V vs. NHE @ pH=7)
$2H_2O + 4h^+ \rightarrow 4H^+ + O_2$	H_2O/O_2	+0.82
$CO_2 + 8e^- + 8H^+ \rightarrow CH_4 + H_2O$	CO_2/CH_4	-0.24
$CO_2 + 6e^- + 6H^+ \rightarrow CH_3OH + H_2O$	CO_2/CH_3OH	-0.38
$2H^+ + 4e^- \rightarrow H_2$	H^+/H_2	-0.41
$CO_2 + 4e^- + 4H^+ \rightarrow HCHO + H_2O$	$CO_2/HCHO$	-0.48
$CO_2 + 2e^- + 2H^+ \rightarrow CO + H_2O$	CO_2/CO	-0.53
$CO_2 + 2e^- + 2H^+ \rightarrow HCOOH$	$O_2/HCOOH$	-0.61
$CO_2 + e^- \rightarrow \cdot CO_2^-$	CO_2/CO_2^-	-1.9

Compared to other photocatalysts, TiO_2 has the advantages of low cost, low toxicity, high chemical and thermal stability, and abundant availability.[7,8] However, realizing TiO_2 assisted CO_2 photoreduction with commercialized devices faces a great difficulty, owing to the complex chemical reaction pathways and unrevealed underlying mechanism.[9] Besides, TiO_2 itself suffers several limitations for CO_2 photoreduction. First, TiO_2 has a large band gap, leading to the low solar energy usage efficiency. Second, the fast charge recombination rate in TiO_2 causes the poor photocatalytic performance[10]. Third, relatively insufficient CO_2 adsorption capability results in the low production rate of solar fuels.

1.2 Summary and Literature Review

Literature research has been focused on designing the innovative nanostructure, and composite materials to address the limitation of TiO_2 from the following aspects: (1) crystal structure, (2) exposed facets (3) defect property and (4) absorbent modification.

Anatase, brookite, and rutile are naturally existing TiO_2 polymorphs.[14-17] Anatase based catalysts have been demonstrated to be highly active, while rutile is less active,[18,19] mainly due to the fast e^- and h^+ recombination in rutile.[20] Brookite is rarely studied in photocatalysis likely due to the past difficulties in synthesizing high purity brookite because of its metastable property.[21-24] A few studies demonstrated the high activity of brookite in photocatalytic oxidation applications.[25,26] Our previous study[3] was the first one to investigate the activity of pure brookite TiO_2 for CO_2 photoreduction with water; brookite showed higher activity than rutile, and surface-defective brookite was even more active than anatase.

Analogous to anatase/rutile mixed-phase TiO_2, anatase/brookite heterojunctions are expected to enhance charge separation as well, probably even superior to anatase/rutile. Possible reasons are: (1) our previous study[3] has discovered that brookite itself is more active than rutile in CO_2 photoreduction; (2) the CB edge of brookite is slightly above that of anatase,[27] making it possible for electrons to transfer from brookite to anatase even in the absence of anatase trapping sites. Some experimental evidence exists in the literature indicating that anatase/brookite mixtures are more active than anatase/rutile mixtures (e.g. P25)[28] and pure anatase[17,29] for photo-oxidation of organic compounds. While bicrystalline anatase/brookite TiO_2 has demonstrated certain

promising photocatalytic oxidation abilities, the relationship between phase composition and catalytic activity is not clear. In the case of anatase and rutile mixtures, there is an optimum phase content (i.e., anatase/rutile = 77/23) that corresponds to the highest photoactivity.[30,31] The optimum phase composition in an anatase/brookite has never been explored; moreover, no studies have been reported on its application in CO_2 photoreduction and the correlation of material properties with photocatalytic activities.

Except for crystal phases, the photocatalytic property of TiO_2 is also related to exposed facets. Among the three low-index facets of anatase {100}, {001} and {101}, {100} facets was demonstrated to have a higher photocatalytic ability.[32,33] Both {100} and {001} facets have higher surface energy than {101},[34-36] and have 100% fivefold coordinated Ti (Ti_{5C}). By contrast {101} facets have only 50% Ti_{5C} sites. Ti_{5C} sites are more active than Ti_{6C} sites due to unsaturated coordination of Ti_{5C}, and Ti_{5C} can act as the active sites for CO_2 activation and conversion.[34,37] Meanwhile, both theoretical calculations and experimental results suggested that the {100} is more active than {001}.[38-40] Pan *et al.* tested the photocatalytic H_2 evolution on TiO_2 with different dominant facets, and TiO_2-{100} showed the highest H_2 evolution.[34] In addition, the order of CO_2 photoreduction to methane on different anatase facets was reported as {100} > {101} > {001}.[33] This is because the conduction band (CB) values for {100}, {101}, and {001} are -0.52eV, -0.49eV, -0.45eV, respectively, resulting in the driving force for CH_4 production ($E^0_{(CO2/CH4)}$ = -0.24 eV vs. NHE, pH = 7.0)) in the order of {100} > {101} > {001}. In this work, {100} is used to refer both {100} and {010} facets, since these two surfaces in anatase are isostructural.[41]

Also, oxygen deficient TiO_2 has shown better performance for CO_2 photoreduction compared to pristine TiO_2 because surface V_O can serve as the active sites for CO_2 adsorption[42,43], activation[44,45], and conversion[44,46]. Also, the light absorption of TiO_2 can be improved due to the rising local states under the CB band minimum caused by the V_O.[47] The promising results of combining the advantages of active facets and defect effects in our previous work[37] have inspired the design of novel TiO_2 material with high percentage {100} facets exposed and high density of surface oxygen vacancies. However, as the concentration of the surface defects increases, the local surface states increase[48], which results in the formation of recombination centers near/on the defect sites. To suppress the recombination, a very thin layer (in ångström level) of metal oxide such as ZrO_2[49], Al_2O_3[50] on the surface of semiconductors was applied by atomic layer deposition (ALD). Amorphous Al_2O_3 was popularly used as the surface passivation coating material on Si for solar cell application by two passivation mechanisms: chemical passivation by reducing the interface state density and field effect passivation caused by the fixed charges in the thin film.[51,52] ALD can precisely control the thickness of the Al_2O_3 layer because of the self-limiting reaction of the dosed precursor gasses.[53,54]

To address the poor CO_2 adsorption capability of TiO_2, Surface modification of TiO_2 with stronger CO_2 adsorbent could improve CO_2 adsorption and reduction on TiO_2. Xie et al.[55] added a variety of metal oxides to Pt-loaded TiO_2 for CO_2 photoreduction and discovered a linear correlation between the amount of chemisorbed CO_2 on metal oxides and the CH_4 yield. Our recent study demonstrated that CO_2 photoreduction was significantly improved by using a hybrid adsorbent–photocatalyst (i.e., MgO/TiO_2

microspheres) due to great CO_2 adsorption ability of MgO.[56,57] Layered double hydroxides (LDHs), known as a class of anionic clays or hydrotalcite (HT)-like materials, and their derivatives, e.g. layered double oxides (LDOs) obtained upon calcination of LDHs have both been applied as CO_2 adsorbents. [58-61] LDOs can be reconstructed to LDHs upon rehydration.[62] Our recent work reported an integrated CO_2 capture and photocatalytic reduction process by a hybrid TiO_2/MgAl-LDO material where captured CO_2 on MgAl-LDO can be converted to CO by TiO_2 under UV light irradiation.[63] Hong et al.[64] assembled MgAl-LDHs nanosheets with carbon nitride (C_3N_4) photocatalyst, which was demonstrated to yield more CH_4 from photoreduction of CO_2 than C_3N_4 alone in aqueous solution with Pd as the cocatalyst. The main reason was identified to be the enrichment of CO_2 adsorption on the catalyst surface by MgAl-LDHs. Other LDHs like ZnAl-LDHs, ZnCr-LDHs and NiAl-LDHs did not make significant improvement of CH_4 production since they have very limited CO_2 adsorption capacity.[64]

2. BICRYSTALLINE TiO_2 WITH CONTROLLABLE ANATASE-BROOKITE PHASE CONTENT FOR ENHANCED CO_2 PHOTOREDUCTION[2]

2.1 Introduction

Mixed-phase TiO_2 nanomaterials other than commercial P25 TiO_2 nanoparticles are scarcely studied in CO_2 photoreduction, and the interactions of the different phases during the CO_2 photoreduction reactions have not been explored. It is believed that the junctions between different phases of TiO_2 play a significant role in improving its photo-oxidation activity.[16,17] Several studies have explored the mechanism for the enhanced activity of anatase and rutile mixtures such as P25; however, the findings are not conclusive. Some studies suggested that photoinduced electrons tend to transfer from the higher-level anatase conduction band (CB) to the lower-level rutile CB,[65] while the holes in the anatase valance band (VB) could migrate to the rutile VB.[66] On the contrary, other studies suggested that electrons transfer from rutile to anatase.[20,67-69] Among them, Hurum et al.[20,69] used electron paramagnetic resonance (EPR) spectroscopy to monitor the direction of electron migration; they suggested that electrons transfer from rutile to anatase because the energy levels of the electron trapping sites in anatase are lower than that of the rutile CB. Also, the interfacial sites between anatase and rutile facilitate the electron transport and prevent the recombination of e^- and h^+.[20,69] However, some recent studies

[2] Part of this chapter is reprinted with permission from "Bicrystalline TiO_2 with controllable anatase–brookite phase content for enhanced CO_2 photoreduction to fuels" by Huilei Zhao, Lianjun Liu, Jean M Andino, and Ying Li, 2013. *Journal of Materials Chemistry A*, 1, 8209-8216, Copyright [2013] by the authors.

reported that there are no interactions between the two phases in P25, and anatase and rutile independently catalyze reactions.[70]

According to the literature review in Chapter 1, heterojunction between two crystal phases in the anatase and brookite bicrystalline system can enhance photocatalytic activity for CO_2 photoreduction. In this topic, we have synthesized pure phase anatase, brookite, and mixed-phase anatase/brookite catalysts with a controllable brookite fraction. We have investigated the effect of TiO_2 phase fractions and nanostructures on CO_2 photoreduction, including the optimum phase composition for CO_2 photoreduction. The in situ spectroscopic studies was also conducted to investigate the CO_2 reduction mechanism.

2.2 Materials and Methods

2.2.1 Catalyst Preparation

TiO_2 nanocrystals of single-phase anatase and brookite and mixed-phase anatase/brookite were prepared using a hydrothermal method.[71] In a typical preparation process, 10 ml titanium bis (ammoniumlactate) dihydroxide (50% in H_2O, Sigma-Aldrich), was mixed with 90 ml urea solution (with varying concentration of urea) and sealed in a 250 ml Teflon-lined autoclave, which was then sealed and placed in an electric oven at 160 °C for 24 h. After the hydrothermal process, the autoclave was naturally cooled down to room temperature. The precipitates were centrifuged, washed with de-ionized water, dried at 60°C for 12 h, ground and finally calcined at 400 °C for 3 h. To prepare pure phase anatase, the urea concentration in the precursor solution was 0.1 M. A urea concentration above 0.1 M led to the formation of an anatase/brookite mixture, and

the brookite content increased with the urea concentration. At 7.0 M, pure brookite was formed. Table 2 summarizes the relation between the urea concentration and the phase composition. The prepared TiO_2 mixtures were denoted as A_xB_y, where x and y are the phase fraction of anatase and brookite, respectively.

2.2.2 Catalyst Characterization

The crystal structures of the prepared TiO_2 samples were identified by X-ray diffraction (Scintag XDS 2000) using Cu Kα irradiation at 45 kV and a diffracted beam monochromator operated at 40 mA in the 2θ range from 20° to 50° at a scan rate of 2°/min. The crystallite sizes of catalysts were calculated by the Scherrer Equation. Quantitative phase composition analysis of as prepared TiO_2 was performed using Rietveld refinement method by the MAUD software (version 2.33).[72,73] The XRD data of as prepared TiO_2 samples together with the known standard data of anatase (tetragonal) and brookite (orthorhombic) were loaded into the MAUD software. The isotropic model and anisotropic model were chosen for anatase and brookite, respectively.[72] Peak positions and scale factors were adjusted before quantitative analysis.

Raman spectroscopy was carried out with a Renishaw 1000B system in the range of 100-700 cm^{-1}. The specific surface areas of all synthesized catalysts were obtained by nitrogen adsorption/desorption at 77 K using the Brunauer-Emmett-Teller (BET) method (Micrometrics, ASAP 2020). UV–vis spectra of the catalysts were obtained by a diffuse reflectance UV–vis spectrophotometer (Ocean Optics) using $BaSO_4$ as the background. The morphologies of TiO_2 polymorphs were characterized by Scanning electron microscopy (SEM, Hitachi S4800), using a secondary electron detector (SE) at an

accelerating voltage range of 5~10 kV. Transmission electron microscopy (TEM) and high-resolution transmission electron microscopy (HRTEM) were carried out with 300 keV electrons in a Hitachi H9000NAR instrument with 0.18 nm point and 0.11 nm lattice resolutions, to obtain crystal structure, morphology, and lattice information of TiO_2 nanocrystals.

2.2.3 Photocatalytic Activity Measurement

The photocatalytic reduction of CO_2 over the TiO_2 samples was conducted in a photoreactor operating in a continuous-flow mode. The experimental setup was similar to that described in our previous work.[4] A solar simulator (Oriel, 150 W) was used as the light source. The light intensity was 69.6 mW/cm^2 for $200 < \lambda < 1000$ nm and 12.5 mW/cm^2 for $200 < \lambda < 400$ nm (UV region), as measured by a spectroradiometer (International Light Technologies ILT950). The photoreactor was cylindrical shape with a stainless steel housing and a quartz window (dia. = 7.5 cm). For each test, 100 mg TiO_2 powder catalyst was evenly dispersed onto a glass-fiber filter that was placed at the bottom of the photoreactor facing the light source.

Ultrahigh purity CO_2 (99.999%, Praxair) regulated by a mass-flow controller (MFC) continuously passed through a bubbler that contained de-ionized water. The resulting gas mixture (CO_2 and 2.3 vol% H_2O vapor) was introduced to the photoreactor. A gas chromatograph (GC, Agilent 7890A) equipped with a thermal conductivity detector (TCD) and a flame ionization detector (FID) was used to continuously analyze the gaseous products. A Carboxen-1010 PLOT capillary column coupled with the TCD was used for

CO measurement, and a HP-PLOT-Q capillary column coupled with the FID was used for CH_4 measurement.

2.2.4 In-situ DRIFTS Analysis

To evaluate the interaction of CO_2-H_2O with the photocatalyst ($A_{75}B_{25}$) during the reaction process, in situ diffuse reflectance infrared Fourier transform spectroscopy (DRIFTS) was applied in a simulated reaction condition. The in situ experiments were conducted under such a sequential procedure: (1) the $A_{75}B_{25}$ catalyst was purged with He at 200 ^oC to remove the residual water and hydroxyl groups on the surface, (2) a CO_2/H_2O mixture was continuously introduced to the DRIFTS cell for 30 min when the intensities of adsorption peaks of CO_2 and H_2O reached saturation levels, and (3) the light from the solar lamp was introduced to the DRIFTS cell by a liquid guide. The IR spectra were recorded as a function of time to monitor the surface adsorbed species during H_2O and CO_2 adsorption in the dark (step 2) and the surface intermediates during the photocatalytic reaction process (step 3).

2.3. Results and Discussion

2.3.1 Crystal Structure and Morphology of TiO_2 Polymorphs

The urea concentration in the precursor solution was directly related to the phase content of the prepared TiO_2 nanocrystals (**Table 2**). The crystal structure of TiO_2 with different ratios of anatase/brookite was confirmed by XRD, as shown in **Figure 2a**. The anatase/brookite ratios were calculated by the Rietveld refinement method. **Figure 2b** shows the Rietveld refinement result of $A_{50}B_{50}$ as an example. At the lowest concentration

of urea (0.1 M), pure phase anatase (JCPDS No. 21-1272), i.e., A_{100}, was obtained. With an increasing concentration of urea up to 1.5 M, bicrystalline anatase/brookite mixtures with an increasing brookite fraction, i.e., $A_{96}B_4$, $A_{75}B_{25}$, $A_{50}B_{50}$, and $A_{37}B_{63}$ were formed. At the highest urea concentration (7.0 M), pure brookite (JCPDS No. 29-1360) was obtained. The existence of brookite in the resultant powders is readily discernible from its unique (121), (221), and (032) diffraction peaks at 30.81, 42.34, 46.07° (2θ), respectively (**Figure 2a**). Clearly, through adjusting the concentration of urea, anatase, brookite or mixtures with controllable anatase/brookite phase fractions were successfully prepared.

Table 2 The characteristics of prepared TiO_2 catalysts including crystal phase content, BET specific surface area, pore size and pore volume, band gap, and the corresponding urea concentration in the precursor solution during material synthesis.

Catalyst	Urea Conc. (M)	Anatase Phase (%)	Brookite Phase (%)	BET Specific Surface Area (m^2/g)	Pore Size (nm)	Pore Volume (cm^3/g)	Band Gap (eV)
A_{100}	0.1	100	0	145.6	6.2	0.23	3.08
$A_{96}B_4$	0.25	96	4	134.5	5.9	0.20	3.12
$A_{75}B_{25}$	0.5	75	25	140.3	5.5	0.20	3.15
$A_{50}B_{50}$	1.0	50	50	84.5	7.0	0.18	3.15
$A_{37}B_{63}$	1.5	37	63	70.2	10.7	0.19	3.20
B_{100}	7.0	0	100	76.6	18.4	0.35	3.22

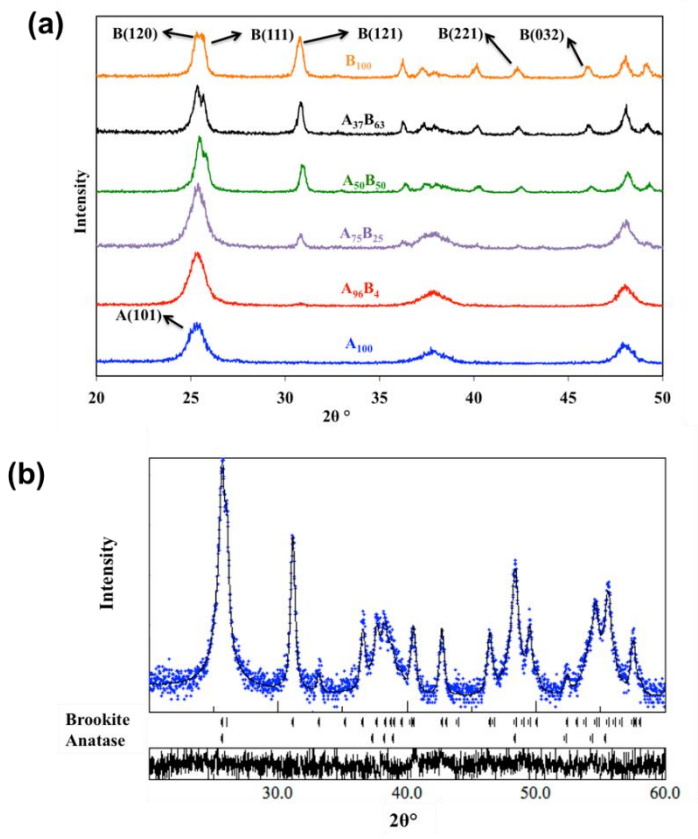

Figure 2 XRD patterns of the prepared TiO_2 catalyst powders with different fractions of anatase and brookite phases (a); Rietveld refinement result for the $A_{50}B_{50}$ sample (b).

The morphologies of the prepared TiO_2 nanocrystals were examined by SEM, as shown in **Figure 3**. Pure anatase, A_{100}, consisted of agglomerate sphere-shaped nanoparticles, while pure brookite, B_{100}, was rod-shaped nanoparticles. For anatase/brookite mixtures, the brookite nanorods appeared to have a lower aspect ratio (brick-shaped) than those observed in pure brookite (rod-shaped). With an increasing brookite fraction in the anatase/brookite mixtures, the number of nanobricks/nanorods increased and the size became larger. Eventually, the brookite crystals evolved from nanobricks to nanorods as the brookite content approached 100%.

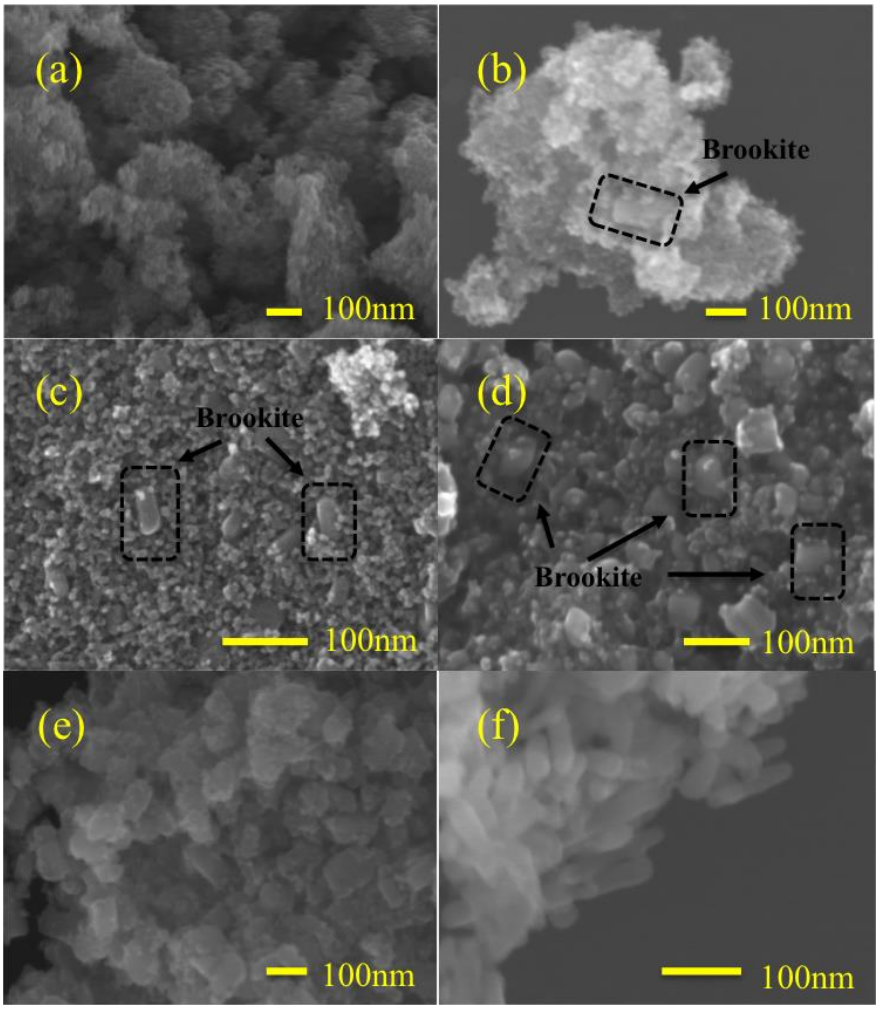

Figure 3 SEM images of A_{100} (a), $A_{96}B_4$ (b), $A_{75}B_{25}$ (c), $A_{50}B_{50}$ (d), $A_{37}B_{63}$ (e) and B_{100} (f). The circled areas in black indicate brookite nanobricks.

The particle size, morphology, and lattice structure of $A_{75}B_{25}$ were further evaluated by TEM and HRTEM, as shown in **Figure 4**. A mixture of spherical and rod-shaped nanoparticles were observed (**Figure 4a**). The spherical particles are in the range of 5~10 nm and the nanorod has a width of 20 nm and length of 60 nm. HRTEM images in **Figure 4 b-c** clearly demonstrated that the spherical nanoparticle was anatase (lattice

spacing = 0.35 nm, corresponding to the (101) plane) and the nanorod was brookite (lattice spacing = 0.91, 0.35 nm, corresponding to (100) and (210) plane, respectively).[3]

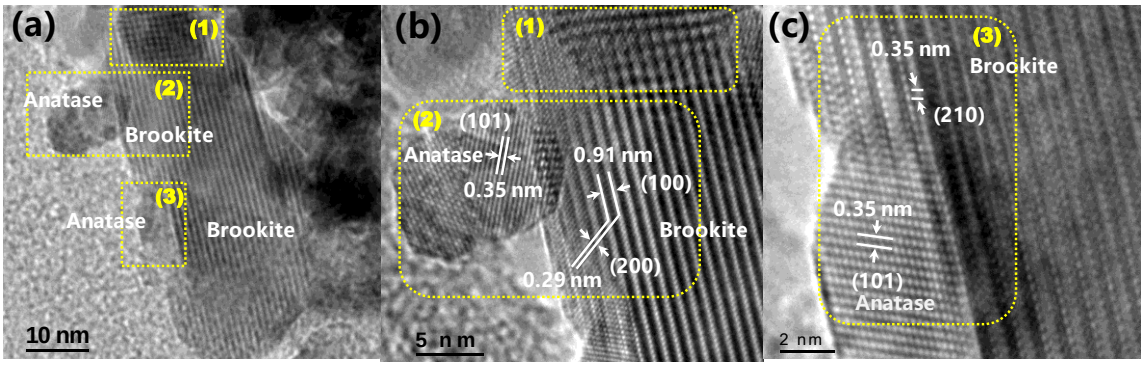

Figure 4 TEM images of $A_{75}B_{25}$ (a), and HRTEM images of $A_{75}B_{25}$ (b, c).

Figure 4b-c also demonstrated the overlapping anatase and brookite particles and the interface between them. In **Figure 4b** the lattice fringe becomes fuzzy and even discontinued (Region 1) where the anatase and brookite crystals overlap. An anatase particle was also located at the edge of brookite (Region 2). Besides those simple attachments of anatase particles to brookite particles, a coherent interface between anatase and brookite could be formed. As shown in **Figure 4c**, the lattice spacing of the anatase (101) plane matches that of the brookite (210) plane (0.35 nm) in the region where the two particles overlap (Region 3). This observation agrees with theoretical simulation results that the brookite (210) surface and the most stable anatase (101) plane have the same type of building block, and both phases may share a common boundary.[74] On anatase (101) all the octahedron units are closely packed, while on brookite (210) the rotated units are closely packed only along the [001] direction.[74] This difference may cause a distortion at the interface between the two crystal phases. The HRTEM images in **Figure 4**

demonstrated that when anatase and brookite nanocrystals grow in the same orientation, a unique interface between them could be possibly formed.

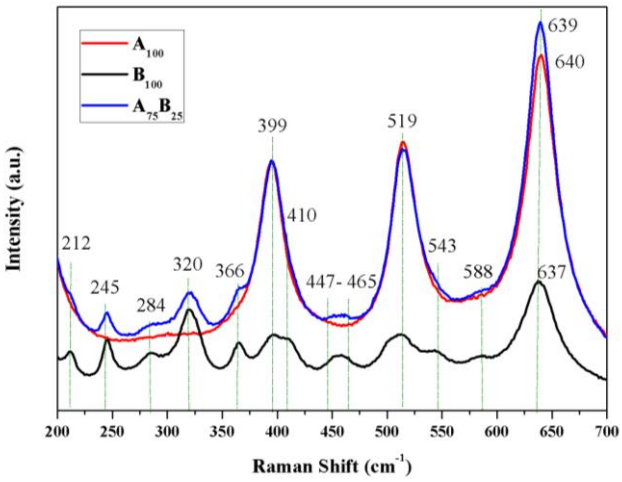

Figure 5 Raman spectra of A_{100}, B_{100}, and $A_{75}B_{25}$ samples.

Raman spectra (**Figure 5**) have further proved the existence of both anatase and brookite crystals in the A/B mixture ($A_{75}B_{25}$). Brookite has the most intense Raman bands at ~245, ~320, ~399, ~410, and ~637 cm^{-1}, while anatase has intense Raman bands at ~399, ~519, and ~639 cm^{-1}.[75] As compared with the spectra of A_{100} and B_{100}, the Raman spectrum of $A_{75}B_{25}$ included all the bands of the two crystal phases, thus indicating a mixed phase of anatase and brookite.

2.3.2. Textural and Optical Properties of TiO_2 Polymorphs

Figure 6 shows that the N_2 adsorption/desorption isotherms for all the six TiO_2 samples are Type IV, characteristics of materials with mesoporous structures. The isotherms of B_{100} and $A_{37}B_{63}$ have a similar shape and close at a higher relative pressure compared to those of A_{100}, $A_{96}B_4$, $A_{75}B_{25}$, and $A_{50}B_{50}$. Correspondingly, the calculated

pore sizes of anatase-rich TiO_2 are smaller than those of brookite-rich TiO_2 (**Table 2**).

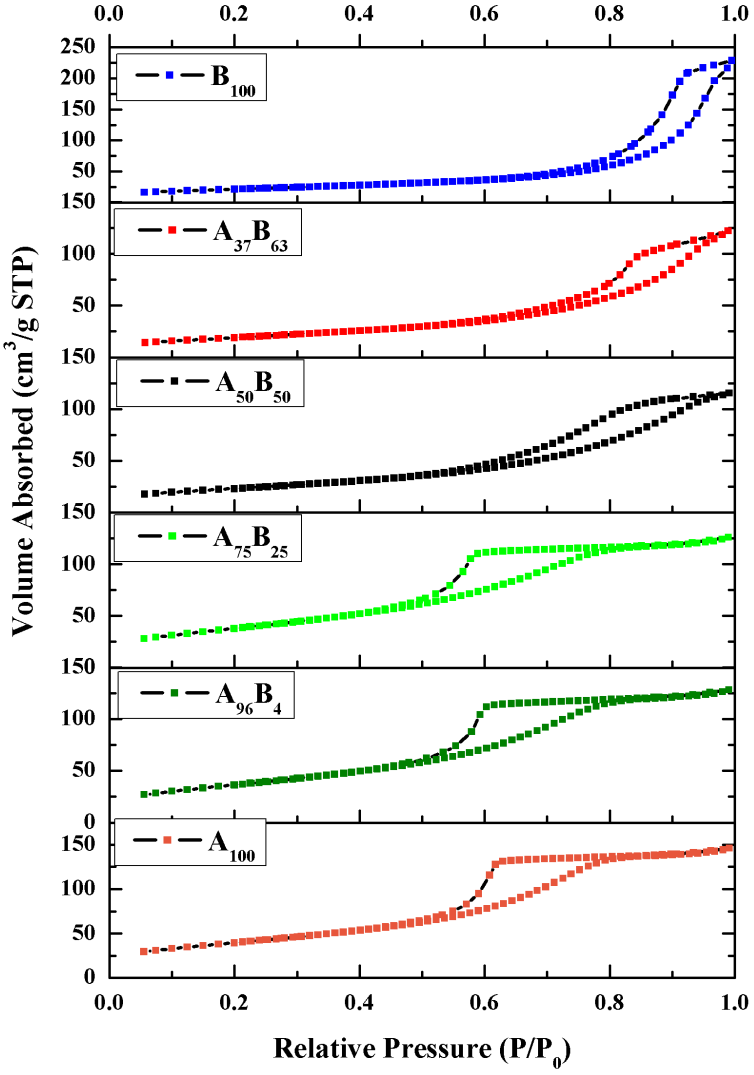

Figure 6 Nitrogen adsorption-desorption isotherms for the prepared TiO_2 catalysts

This is because the inter-particle spaces between the agglomerated anatase TiO_2 nanoparticles were smaller than those between the nanobricks/nanorods in brookite-rich TiO_2. **Table 2** also compared the BET specific surface areas of the various TiO_2 catalysts. The surface areas of anatase and anatase-rich samples (A_{100}, $A_{96}B_4$, and $A_{75}B_{25}$) were close

(around 140 m^2/g) and were twice as much as those of brookite-rich and pure brookite TiO_2 ($A_{37}B_{63}$ and B_{100}). The sharp decrease in surface area from $A_{75}B_{25}$ to $A_{50}B_{50}$ can be explained from their SEM images in **Figure 3**: for $A_{75}B_{25}$, brookite nanobricks are embedded in agglomerated anatase nanoparticles; whereas, for $A_{50}B_{50}$, a smaller amount of anatase nanoparticles are dispersed on the surfaces of brookite nanobricks. The surface area of the larger brookite crystals is smaller than that of the smaller anatase crystals.

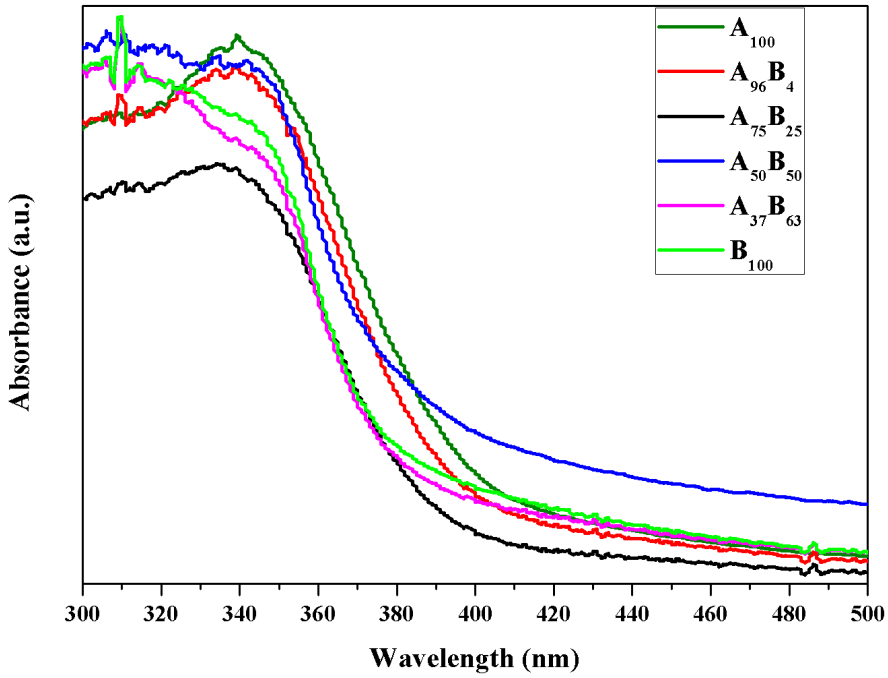

Figure 7 The UV-Vis diffuse reflectance spectra (displayed in absorbance) of the prepared TiO_2 catalysts.

Figure 7 compares the UV-vis spectra, displayed in absorbance units, of the prepared TiO_2 catalysts. The absorption edge of A_{100} is around 402 nm, corresponding to a band gap at 3.08 eV, close to the value reported in the literature.[3,76] An increase in the brookite fraction in the anatase/brookite mixture results in a blue shift in the absorption

spectra and an increase in the band gap (listed in **Table 2**). B_{100} has the largest band gap at 3.22 eV. The observed larger band gap of brookite than anatase agrees with that reported in the literature,[25] as the conduction band of brookite is positioned at 0.14 eV more negative than that of anatase.[77] The band gaps stayed the same before or after 4 hours photo illumination.

2.3.3 Photocatalytic Activity for CO_2 Reduction

The photocatalytic activities of the prepared TiO_2 catalysts were tested for CO_2 photoreduction with H_2O vapor. Background experiments were first conducted under the following conditions: (1) blank glass-fiber filter in the reactor without loading catalysts under the irradiation of solar simulator in a CO_2+H_2O flow; (2) catalysts loaded on a glass-fiber filter in the dark in a CO_2+H_2O flow; and (3) catalysts loaded on a glass-fiber filter under simulated solar radiation in a He+H_2O flow. In all cases, no carbon-containing products were detected. These background tests indicated that any carbon-containing products formed (described in the subsequent part of this paper) were generated solely from the reaction of CO_2+H_2O over the photocatalysts under light irradiation, not from any surface impurities on the catalysts.

As consistent with our previous studies,[2, 3] CO was the major product and CH_4 was the minor product formed during CO_2 photoreduction with H_2O vapor, and no other products (such as H_2) were detected. The absence of H_2 production was consistent with the literature that H_2 production is prominent only in the presence of noble metal co-catalysts (e.g., Pt, Ag)[4,78] or in the presence of sacrificial agents (e.g., CH_3OH).[4,79] CH_4 production was much lower than CO production, likely because the formation of CH_4

requires the complete reduction of CO_2 to C, and a subsequent reaction with available H atoms from the decomposition of water vapor on the same catalyst surface. If the CO desorbs from the surface before it can be fully reduced, then the formation of CH_4 is impacted.

Figure 8 compares the apparent production rates of CO on various TiO_2 catalysts. The test for each sample was repeated twice (a fresh catalyst was used each time), and the errors were within reasonable experimental uncertainties. The CH_4 production rates are not plotted in Figure 8 because they were too low (in the range of 0.001~0.005 μ mol h^{-1}) and did not vary significantly for different catalysts. B_{100} had the lowest activity among all the catalysts, with a CO production rate at 0.073 μmol h^{-1}. A_{100} had a CO production rate at 0.123 μmol h^{-1}, higher than that of B_{100}.

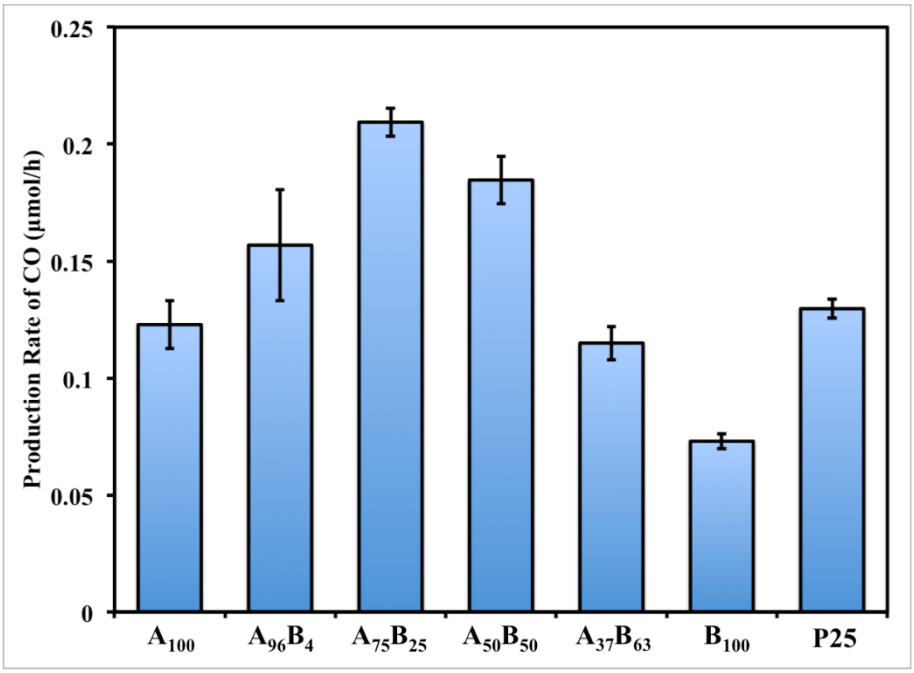

Figure 8 The production rates of CO using various TiO_2 catalysts (the reactants were a gas mixture of 97.7 vol% CO_2 and 2.3 vol% H_2O).

The bicrystalline samples with dominating anatase phase ($A_{96}B_4$ and $A_{75}B_{25}$) or equal anatase-brookite content ($A_{50}B_{50}$) were the most active ones, having a CO production rate from 0.157 to 0.209 μmol h^{-1}. The activity of $A_{75}B_{25}$ was nearly twice as high as that of A_{100} and three times as high as that of B_{100}. Further increasing the brookite content (i.e., brookite-rich $A_{37}B_{63}$) led to a lower CO production rate at 0.115 μmol h^{-1}. Commercial TiO_2 P25 was also tested as comparison; it had a CO production rate of 0.130 μmol h^{-1}, lower than the anatase-rich bicrystalline anatase/brookite samples. The above results demonstrate that the anatase-rich bicrystalline anatase/brookite mixtures are superior to single crystalline anatase or brookite and anatase/rutile mixtures (i.e., P25). Considering that pure anatase A_{100} had the largest specific surface area and the smallest band bap (**Table 2**), the higher activity of bicrystalline anatase/brookite is very likely ascribed to the interactions between the anatase and brookite nanocrystals. This interaction between anatase and brookite seems to be more effective than that between anatase and rutile (as in P25). In addition, it is reasonable to find that anatase-rich A/B mixtures are more active than brookite-rich A/B mixtures since pure anatase is more active than pure brookite.

The experimental results in **Figure 8** indicate that anatase rich A/B mixture with 75% anatase and 25% brookite, i.e., $A_{75}B_{25}$ is the most active among all the prepared catalysts. There are three possible reasons for its superior activity: (1) the more negative CB band of brookite may induce electron transfer from brookite to anatase, thus enhancing charge separation; (2) the facilitated formation of the intrinsic defect sites in brookite may enhance electron trapping,[3,80] and (3) the distorted interfaces between anatase and brookite

crystals (as evidenced in the HRTEM images) may facilitate interfacial electron transport and prevent the recombination of electron-hole pairs.[81]

Additional experiments were conducted to explore the potential O_2 production from H_2O oxidation using the sample of anatase-rich $A_{75}B_{25}$. Prior to the photocatalytic reaction, the photoreactor was purged with a CO_2/H_2O gas mixture to eliminate the air inside the reactor. However, even after purging for a few hours, there was still background O_2 (in a few hundred ppm range) together with N_2 detected in the reactor effluent gas. Hence, a better indicator of O_2 production by the catalyst is the volumetric ratio of O_2/N_2 in the effluent gas, as also suggested in the literature and in our previous work.[2,82]

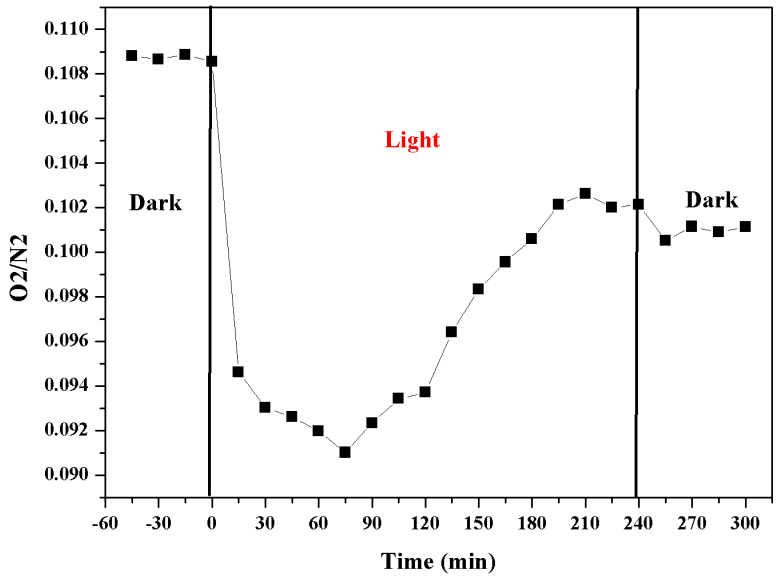

Figure 9 Time dependence of the volumetric ratio of O_2/N_2 before, during and after the photoreduction of CO_2 with H_2O on the $A_{75}B_{25}$

Figure 9 shows the O_2/N_2 ratio before, during and after the photoreaction, when the reactor effluent gas was sampled every 15 min. Before turning on the light (in the dark), the O_2/N_2 ratio was steady. Immediately upon photo-illumination, the O_2/N_2 ratio

dramatically decreased in the first 60 min and then gradually increased. The sharp decrease is probably due to the consumption of residual O_2 in the reactor through the reaction with photogenerated electrons $O_2 + e^- \rightarrow O_2^-$ and consecutive reactions.[2] The gradual increase in the O_2/N_2 ratio after 60 min photo irradiation indicated the generation of O_2 through oxidation of H_2O with photogenerated holes, $H_2O + 2h^+ \rightarrow 2H^+ + (1/2)\ O_2$. Because the increasing amount of generated O_2 overweighed the previous concurrent O_2 consumption process, the net result was that the O_2/N_2 ratio gradually increased with time and finally reached in a steady state after 200 min. After turning off the light (the second dark period), the O_2/N_2 ratio dropped. This result again verified the generation of O_2 during the photocatalytic CO_2 reduction with H_2O vapor process.

2.3.4 In-situ DRIFTS Investigation on Surface Chemistry and Reaction Intermediates

As shown in **Figure 10**, in the dark, CO_2/H_2O adsorption on $A_{75}B_{25}$ resulted in the formation of bicarbonate (HCO_3^-, 1220 and 1420 cm^{-1}), bidentate carbonate (b-CO_3^{2-}, 1360 and 1570 cm^{-1}), monodentate carbonate (m-CO_3^{2-}, 1300 and 1540 cm^{-1}), and carboxylate (CO_2^-, 1250 and 1673 cm^{-1}).[2,83,84] The intensities of the peaks remained almost unchanged from 20 min to 30 min, indicating that the adsorption of CO_2/H_2O reached the saturated level on the surface of $A_{75}B_{25}$. Immediately upon photo-irradiation for 15 min, the peaks for HCO_3^- and CO_2^- species decreased or even disappeared, while the peak for surface H_2O (1639 cm^{-1})[2] and CO_3^{2-} increased. Upon increasing the photo-illumination time from 15 min to 3 h, the intensities of the H_2O and CO_3^{2-} peaks gradually increased, while that of HCO_3^- was gradually decreased and CO_2^- completely disappeared.

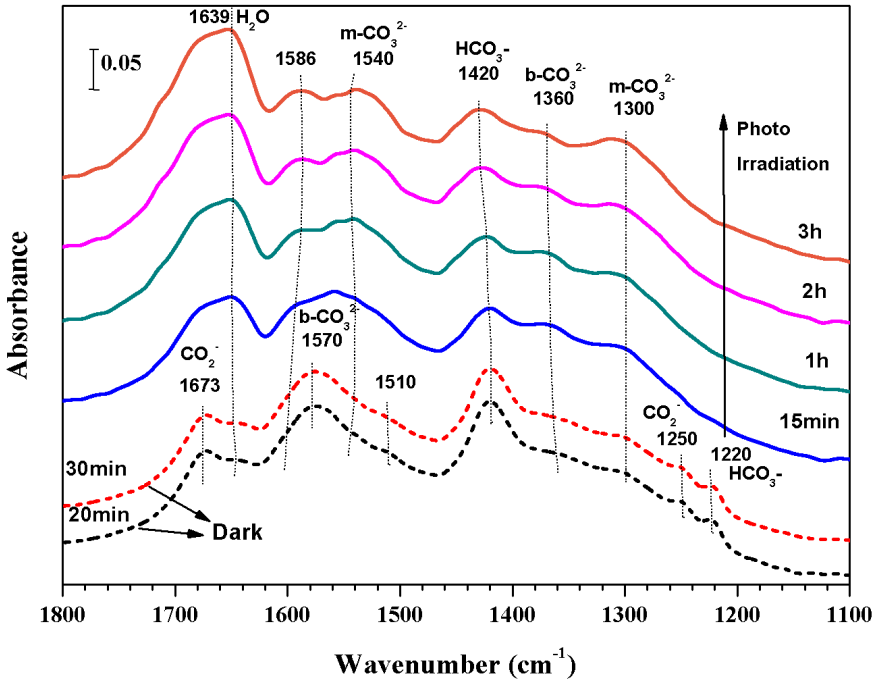

Figure 10 In situ DRIFTS spectra of CO_2 and H_2O adsorption on $A_{75}B_{25}$ for 30 min in the dark (short-dash lines), and subsequent photoreduction process under the UV-vis light irradiation for 3 h (solid lines)

In our previous studies[85], we found that HCO_3^- and CO_2^-, formed from CO_2 interaction with OH groups and Ti^{3+} sites, are the possible intermediates for CO_2 photoreduction to CO and C_1 fuels (e.g., CH_4) once the dissociative H atom is available. The DRIFTS study here again demonstrated the importance of the HCO_3^- and CO_2^- as the CO_2 reduction intermediates, evidenced by the weakened HCO_3^- peak and the disappearance of CO_2^- upon photo-illumination. The increase of CO_3^{2-} species could result from HCO_3^- transformation. The increase in surface H_2O may be explained as follows. It is known that H_2O and CO_2 competitively adsorb on TiO_2. H_2O and CO_2 adsorption reached equilibrium in the dark. Upon photo-illumination, this equilibrium was broken

when adsorbed CO_2 species was reduced to CO and desorbed into the gas phase. Hence, some surface sites like OH groups became available for incoming gas molecule adsorption. Because H_2O has a higher binding energy with surface OH groups than CO_2, once the OH groups were re-exposed, most of them may be occupied by H_2O, and thus preventing subsequent CO_2 adsorption on the surface. The lack of continuous formation of active CO_2 adsorption species (HCO_3^- and CO_2^-, not CO_3^{2-}) species may cause the observed catalyst deactivation over a few hours observed in the photocatalytic activity measurements. The above described DRIFTS results have provided significant insights into the reaction mechanism and catalyst deactivation which have been rarely studied in the literature.

2.4 Conclusions

Anatase-rich anatase/brookite mixtures showed superior activity for the photocatalytic reduction of CO_2 to fuels. The interfaces between anatase and brookite nanocrystals are believed to enhance photo-induced charge transfer and electron-hole separation, and thus they are more active than single-phase anatase or brookite. Anatase-rich A/B mixtures are more active than brookite-rich A/B mixtures since the anatase nanoparticles used in this study have higher specific surface area and smaller band gaps than the brookite nanorods that were used. The anatase-rich A/B mixture ($A_{75}B_{25}$) was far more active than the anatase-rich A/R mixture with similar anatase fraction (i.e. P25). This important finding suggests a new direction for the development of efficient catalysts for CO_2 photoreduction to fuels, i.e. brookite-containing mixed phase TiO_2 nanocrystals.

3. CO_2 PHOTOREDUCTION WITH WATER VAPOR BY Ti-EMBEDDED MgAl LAYERED DOUBLE HYDROXIDES[3]

3.1 Introduction

A general pathway for TiO_2 assisted CO_2 photoreduction with H_2O was described as follows: reactants adsorbed on the surface of TiO_2, photogeneration of electrons and holes, activation of the adsorbed reactants by charge carriers, formation of intermediates adsorbed on the surface of TiO_2, conversion of intermediates to products, desorption of products from catalyst surface, and regeneration of the catalyst.[86] However, fast recombination rate of photogenerated electrons and holes, and poor CO_2 adsorption capability on the surface of TiO_2 limit its photocatalytic activity. Surface modification of TiO_2 with stronger CO_2 adsorbent could improve CO_2 adsorption and reduction on TiO_2. LDHs themselves have also been demonstrated as photocatalysts thanks to their highly tunable chemical compositions. Silva et al.[87] reported O_2 evolution from water under visible light on ZnTi, ZnCr and ZnCe-LDHs. Parida et al.[88] reported photocatalytic H_2 generation from water by a MgAlFe-LDH. Ti-containing LDHs (NiTi, ZnTi and MgAlTi-LDHs) have been reported to enhance H_2 production from photocatalytic water splitting by providing highly dispersed TiO_6 units in the LDHs structure.[89] In general, Ti species in MgAlTi-LDHs remain as amorphous phase in LDHs prepared by a conventional coprecipitation method.[62] However, reconstructed LDHs, prepared by calcination at 400

[3] Part of this chapter is reprinted with permission from "CO_2 photoreduction with water vapor by Ti-embedded MgAl layered double hydroxides" by Huilei Zhao, Jinye Xu, Lianjun Liu, Guiying Rao, Cunyu Zhao, and Ying Li, 2016. *Journal of CO_2 Utilization*, 15, 15-23, Copyright [2016] by Elsevier B.V.

°C and subsequent rehydration in water showed crystalline TiO_2 in MgAlTi-LDHs.[62] While both MgAlTi-LDHs (with amorphous Ti species) and crystalline TiO_2 embedded in MgAl-LDH are demonstrated as photocatalysts, it is not clear in the literature which material is more active, particularly for CO_2 photoreduction with water.

According to the literature review in Chapter 1, the photocatalytic activity for CO_2 reduction can be improved by modifying TiO_2 with CO_2 adsorbent. In this work, we have prepared three types of MgAlTi-LDHs photocatalyst materials with different Ti species and structures and compared their activities in CO_2 photoreduction with water. The first type is prepared using a conventional coprecipitation method. The second method is coprecipitation followed by hydrothermal treatment to increase the crystallinity of TiO_2. This method has not been reported in the literature before and is inspired by the idea that amorphous TiO_x species can be transformed to crystalline TiO_2 by hydrothermal treatment.[90,91] The third method is to reconstruct LDHs by calcination and rehydration, which was anticipated to crystalize TiO_2 while maintaining the layered structure. We have carefully characterized the three types of materials and correlated their materials properties with their photocatalytic activities in CO_2 reduction.

3.2 Materials and Methods

3.2.1 Material Preparation

The first type of MgAlTi-LDH was fabricated with a coprecipitation method reported by Lu et al.[62] In a typical preparation process, solution A containing 1.6 M NaOH and 0.16 M Na_2CO_3 and solution B containing 0.6 M $Mg(NO_3)_2 \cdot 6H_2O$, 0.2 M

$Al(NO_3)_3 \cdot 9H_2O$, and 0.3 M $TiCl_4$ were prepared in two separated beakers. Then solution A was added dropwise into solution B with rigorous stirring until pH 10. The resultant white mixture was aged in a silicon oil bath of 60°C for 18 h. The precipitates were then collected by vacuum filtration and dried overnight at 80°C. The powders were finally grinded and sieved. The atomic ratio of Mg: Al: Ti was 6:2:3. The as synthesized Ti-containing MgAl-LDHs from coprecipitation was denoted as **MgAlTi(CP)** or simply **CP**.

The MgAlTi(CP) powders were re-dispersed in water (1wt%) and stirred for 30 min. Then the mixture was transferred into a hydrothermal vessel and heated at varies temperature (100, 150, or 200°C) for 24 h. After the hydrothermal reaction, powders were obtained by filtration, vacuum drying and grinding. The samples were denoted as **MgAlTi(HT100)**, **MgAlTi(HT150)**, and **MgAlTi(HT200)** or simply **HT100**, **HT150** and **HT200**, where the number designates the hydrothermal temperature.

The MgAlTi(CP) powders were first calcined in a muffle furnace at 400, 500, or 600°C for 2 h and then dispersed in water and rigorously stirred at room temperature for 24 h for reconstruction. Powders were collected after filtering and drying at 80°C. The samples were denoted as **MgAlTi(R400)**, **MgAlTi(R500)**, and **MgAlTi(R600)** or simply **R400**, **R500** and **R600**, where the number designates the calcination temperature.

3.2.2 Material Characterization

Crystal structures of samples were characterized with X-ray diffraction (XRD, Scintag XDS 2000) using Cu Kα irradiation (λ=0.1540562 nm) at 45 kV and a diffracted beam monochromator at 40 mA in the 2θ range of 5°-70° at a scan rate of 2°/min. UV−visible diffuse reflectance spectra (UV−vis DRS) were obtained by an UV−visible

spectrometer (Ocean Optics) using $BaSO_4$ as the background. Scanning electron microscopy (SEM) (Hitachi S4800) was used to visualize the catalyst morphology. Porous textual characterization was performed with nitrogen adsorption–desorption at 77 K using the Brunauer–Emmett–Teller (BET) method for surface area estimation and Barrette-Joynere-Halenda (BJH) method for cumulative pore volume analysis (Micrometrics, ASAP 2020). CO_2 adsorption capacity of different samples were investigated by CO_2 adsorption isotherms taken with the thermogravimetric analyzer (TGA-DAT-2960 SDT). For each test, 15-20 mg of sample was loaded in an Al_2O_3 container and heated to 150°C at a ramp of 10°C/min under an argon flow (100 ml/min). After the weight was stabilized, the argon flow was replaced with a moisturized CO_2 flow (120 ml/min). The weight versus time was recorded and analyzed. Thermal stability analysis of the MgAlTi(CP) material was also carried out on the same thermogravimetric analyzer (TGA) at a heating ramp of 10°C/min from room temperature to 800°C in air flow. Temperature programed desorption (TPD) of CO_2 (10°C/min) was recorded with a mass spectrometer (MS). To characterize the surface chemistry of the MgAlTi(CP) under thermal treatment, Fourier transform infrared spectra (FTIR) were recorded on a Nicolet 6700 spectrometer (Thermo Electron) equipped with a liquid nitrogen-cooled HgCdTe (MCT) detector. The sample was loaded in a reaction chamber (Harrick Scientific, HVCDRP) equipped with a heater and a programmed temperature controller, as well as cooling water circulation.

3.2.3 Activity Tests for CO_2 Photoreduction

For each CO_2 photoreduction test, 50 mg of samples were dispersed on a clean glass fiber filter paper and loaded on the inner wall of a quartz tube reactor. CO_2 (99.999%,

Praxair) controlled by mass flow controller (MFC) was continuously passed through a water bubbler to allow a mixture of CO_2 and 2.3 vol% H_2O vapor to flow through the photoreactor. A 400 W UV lamp (Oriel) was used as the light source, and the light intensity is about 420 mW cm^{-2} in the range of 200-1000 nm. Our previous studies found that slightly increasing the reaction temperature could aid desorption of the surface intermediates and thus promote the photocatalytic reduction of CO_2 with water vapor.[56,57] Therefore, in this work two 250 W infrared lamps were applied to heat up the photoreactor to a temperature of 150°C, the optimal temperature found in our previous work.[56] The photoreactor was operated in a continuous-flow mode, and the gaseous products in the reactor effluent were continuously analyzed by a gas chromatograph (GC, Agilent 7890A) equipped with both a thermal conductivity detector (TCD) and a flame ionization detector (FID).

3.3 Results and Discussion

3.3.1 Crystal Structure and Morphology

Crystal structures of MgAlTi-LDH samples were examined by XRD as shown in **Figure 11**. The XRD pattern of MgAlTi(CP) sample shows peaks at 2θ around 12° (003), 23° (006), 35° (009)/(102), 61° (110) and 64° (113) that match the typical rhombohedral structure of MgAl-LDHs reported in literature.[64,92] The basal spacing corresponding to (003) plane is calculated to be 0.759 nm using Bragg's equation.[93] Assuming 3-layer rhombohedral (3R) stacking sequence[94] of MgAlTi-LDHs, the unit cell parameter *c* was calculated to be 2.276 nm, three times that of the layer-to-layer distance. By applying

Bragg's equation to (110) plane, the unit cell parameter *a* was obtained to be 0.305 nm, which is the averaged metal-to-metal distance within the layers. These calculated parameters were comparable to those reported in the literatue.[95,96] By applying the Scherrer equation on the (003) peak, the crystallite size, i.e. disk diameter [97] in the stacking direction of the MgAlTi(CP) sample was determined to be 8.3 nm.

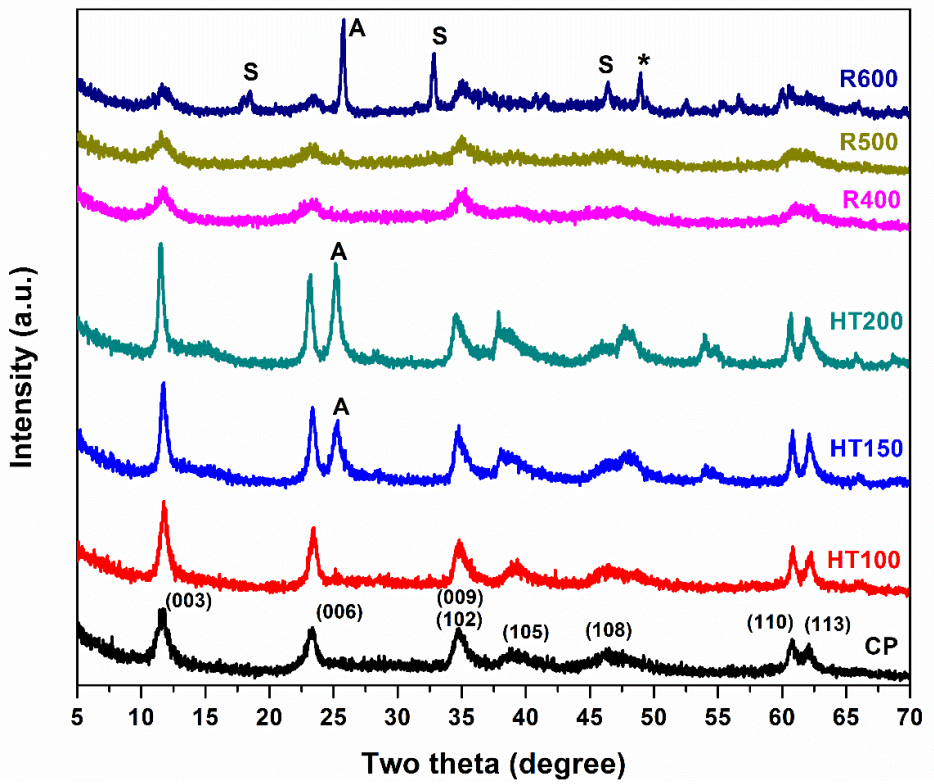

Figure 11 XRD patterns of MgAlTi(CP), MgAlTi(HT100), MgAlTi(HT150), MgAlTi(HT200), MgAlTi(R400), MgAlTi(R500), and MgAlTi(R600) samples. (* refers to Al_2O_3 phase; S refers to spinel $MgAl_2O_4$; A refers to anatase TiO_2)

Figure 11 also shows the crystal structure changes of MgAlTi(CP) treated with hydrothermal or calcination/reconstruction. The (101) diffraction peaks for anatase type TiO_2 (JCPDS no. 21-1272) appeared for HT150, HT200 and R600 samples at 2θ=25.3°, 25.2° and 25.7°, respectively. Hydrothermal at lower than 150 °C or calcination lower

than 600 °C did not result in anatase TiO_2 formation. Yanagisawa et al.[90] attributed the reason that crystallization temperature required in hydrothermal condition was lower than that in calcination in air to the acceleration of nucleation by water. At a higher hydrothermal temperature, the nucleation by structural rearrangement of the TiO_6 octahedral units in the amorphous TiO_2 might proceed quickly and heterogeneously followed by immediate growing, leading to larger anatase crystals.[98] That explains why the anatase crystallite size for HT(200), 12.3 nm, is larger than that of HT(150) 8.4 nm. Reconstructed LDHs generally preserved the original LDH structure, as seen in the R400, R500 and R600 samples; however, reflection peaks of impurities like Al_2O_3 and spinel $MgAl_2O_4$[99-101] were identified on the R600 sample, indicating permanent structure change due to high temperature calcination.

Table 3 Crystal structural parameters of samples

Sample	CP	HT100	HT150	HT200	R400	R500	R600
d(003) (nm)	0.759	0.751	0.753	0.767	0.751	0.758	0.759
(003) disk diameter (nm)	8.3	11.9	14.4	19.9	4.8	5.5	6
a (nm)	0.305	0.304	0.304	0.305	0.303	0.304	0.306
Anatase crystallite size (nm)	/	/	8.4	12.3	/	/	30.1

Crystal structural parameters of MgAlTi-LDHs samples calculated from XRD results were summarized in Table 3.The lattice parameters of LDHs structures remained

similar after hydrothermal and reconstruction treatments, basal spacing d(003) = 0.751~0.767 nm and unit cell parameter a = 0.303~0.306 nm, consistent with the literature.[62] But the crystallinity changed significantly (disk diameter = 4.8~19.9 nm). Hydrothermal treatment at 100, 150, and 200 °C increased the crystallite size of LDHs from 8.3 nm to 11.9, 14.4 and 19.9 nm, respectively. Whereas, reconstructed samples at 400, 500, and 600 °C calcination have a decreased crystallite size to 4.8, 5.5 and 6.0 nm. It is highly possible that during hydrothermal treatment, LDHs crystallites prong to grow larger via ostwald ripening.[102] This phenomenon was also reported by Xu et.al[103] that LDHs particles disaggregated at a lower temperature and followed by the growth of LDHs individual crystallite via 3-D process (dissolution, diffusion, and deposition). At a higher temperature, the development of LDHs accelerated could be due to the faster diffusion of ions, e.g. Mg^{II}, Al^{III} cations. Reconstructed samples were prepared by calcination and reconstruction method, using the memory effect of LDHs materials. Amorphous phase is often produced during the calcination-reconstruction process simultaneously,[104] which led to a smaller crystallite size compared with the unmodified LDH materials. Increasing calcination temperature of LDHs samples may boost the agglomeration of crystals, which could give rise to the growing of crystals in the reconstructed LDHs as well.

Morphologies of the samples obtained by SEM are shown in **Figure 12**-**Figure 13**. The pristine CP sample (**Figure 12**) was composed of densely aggregated small nanoflakes (~50 nm). Porous flower-like morphologies were observed for all the hydrothermal and reconstruction treated samples (**Figure 13**). Increasing the hydrothermal temperature resulted in larger flakes with diameters of ~100, ~500 and

~1000 nm for HT100, HT150, HT200, respectively, which matches the increased crystallite size observed in the XRD results (**Table 3**). Whereas, the reconstructed samples (R400, R500, and R600) consisted of relatively small flakes (~100 nm) and no obvious change of flake size was observed with increased calcination temperature.

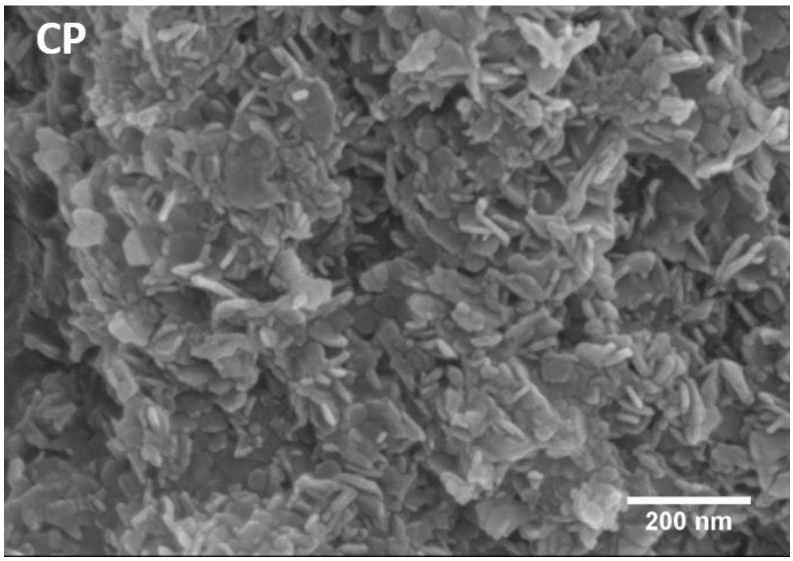

Figure 12 SEM images of MgAlTi(CP)

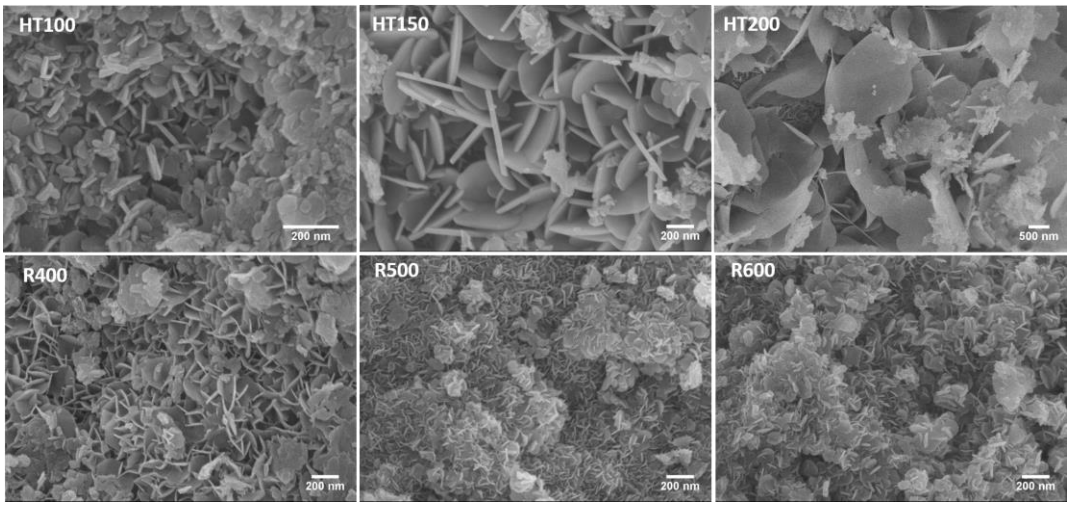

Figure 13 SEM images of MgAlTi-LDHs after hydrothermal treatment (HT100, HT150, and HT200) and calcination + reconstruction treatment (R400, R500, and R600)

3.3.2 Temperature Dependent Properties

To better understand the crystal structural change of the MgAlTi(CP) as a function of calcination temperature, the MgAlTi(CP) sample was calcined at 200, 400, 500, and 600 °C, respectively (without the reconstruction step), and the XRD patterns are shown in **Figure 14(A)**. At a lower temperature (200 °C), broadened LDH characteristic peaks were observed, suggesting that LDH layered structure started to collapse upon thermal treatment.[105] When the calcination temperature was raised to 400-500 °C, the layered structure was completely lost, leaving mixed metal oxide (MMO) of MgO and Al_2O_3. When the calcination temperature further increased to 600 °C, crystal TiO_2 (anatase type, JCPDS no. 21-1272) and spinel phase $MgAl_2O_4$ appeared.

The XRD pattern change of the MgAlTi(CP) sample upon thermal treatment was consistent with TGA result, as shown in **Figure 14(B)**. Three stages with a total weight loss of 34.4% were identified: 20-216 °C, 216-410 °C, and 410-800 °C. In the first stage, water molecules from the material surface and interlayer gallery were lost, but the layered structure was still preserved. In the second stage, dehydroxylation of the brucite-like sheet layers and decarbonation occurred,[97] leading to gradual deformation of the layered structure. In the third stage, carbonates in the interlayer space were further eliminated.[95] Desorption of CO_2 as a result of decarbonation during the heating process (20 to 600 °C with a ramp of 10 °C/min) was recorded as the TPD profile shown in **Figure 14(C)**. The peak centered at 420 °C coincided well with the transition from the second to the third stage weight loss shown in the TGA curve.

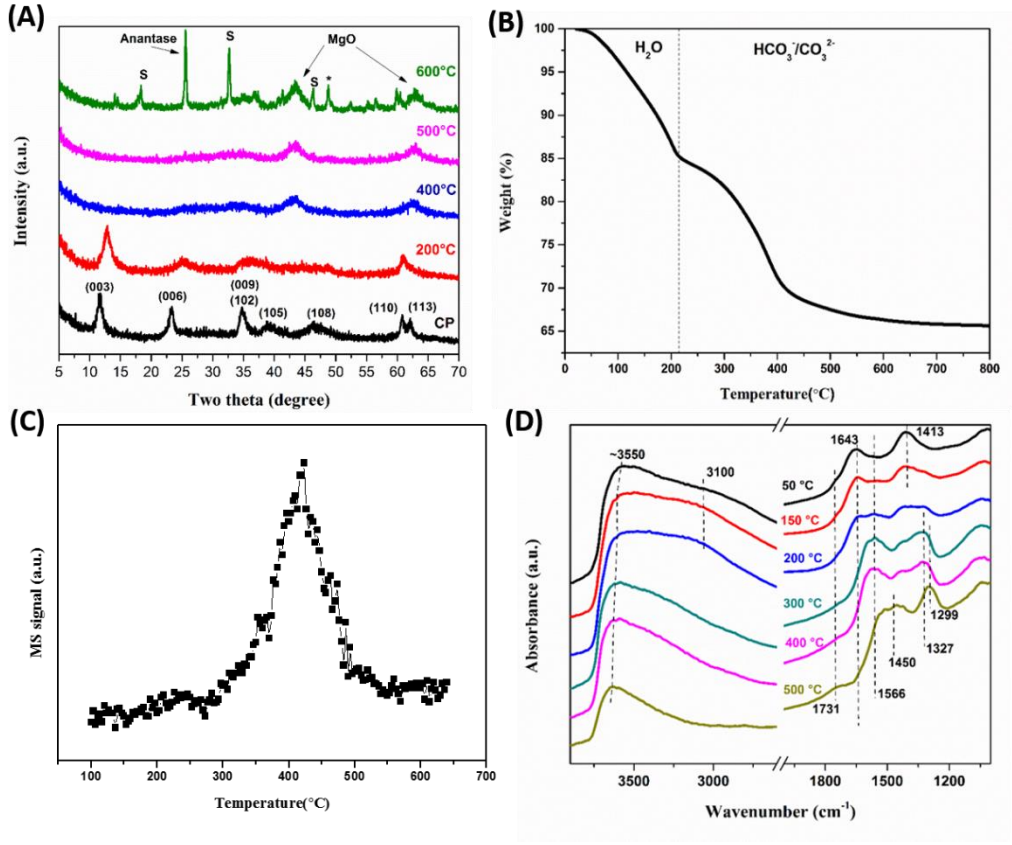

Figure 14 XRD patterns of MgAlTi(CP) after calcined at 200~600°C for 2 h (A); TGA curve of MgAlTi(CP) (B), TPD profile of MgAlTi(CP) for CO_2 desorption (C); and FTIR spectra of MgAlTi (CP) heated at different temperatures in air (D).

FTIR spectra of the sample heated to 50-500 °C (the sample was continuously purged with an air flow) were recorded in **Figure 14(D)**. At 50 °C, the high frequency bands at 3550 and 3100 cm^{-1} were ascribed to vibrations of H_2O and OH^- groups.[95] The band around 1643 cm^{-1} was attributed to bending mode of interlayer water and the one around 1413 cm^{-1} belonged to asymmetric stretching of the interlayer carbonate or bicarbonate.[85,95] As the temperature increased, the 1643 and 1413 cm^{-1} bands gradually decreased and finally disappeared at 300 °C, but new bands at 1566 and 1327 cm^{-1} for bidentate carbonate ($b{-}CO_3^{2-}$)[85] appeared from 150°C and reached the maxima at 300°C.

When the temperature was further raised to 500 °C, bands at 1731, 1450 and 1299 cm^{-1} for bridged carbonate (d-CO_3^{2-})[85] were observed. The FTIR results also agree with the TGA analysis on the structural transformation of the LDH material.

3.3.3 Textual Properties

Table 4 Textual parameters of samples.

Sample	CP	HT100	HT150	HT200	R400	R500	R600
S_{BET} (m^2/g)	169.9	181.4	117	78.3	111.4	102.1	73.8
Pore size (nm)	5.5	6.3	10.8	14.3	4.2	4.4	5.7
Pore volume (cm^3/g)	0.25	0.3	0.38	0.33	0.14	0.16	0.2

Nitrogen adsorption/desorption isotherms were taken at 77K to analyze textual properties of the samples. As shown in **Figure 15A**, all of the samples display a type IV isotherm (IUPAC classification) and type H3 hysteresis loop,[106,107] indicating mesoporous structures formed by aggregates of flakes or slit pores between edged flakes. The relative pressure (P/P_0) at the loop closing point for HT150 and HT200 (0.6-0.7) was higher than that for the rest of samples (~0.4), suggesting larger pore sizes for HT150 and HT200 samples. The BET surface area decreased from 169.9 m^2/g for the CP sample to 117.0 and 78.3 m^2/g at 150 and 200 °C hydrothermal treatment temperatures. However the HT100 sample had slightly increased BET surface area of 181.4 m^2/g. A similar trend was also observed for the reconstructed samples, with the BET surface area decreased to 111.4, 102.1 and 73.8 m^2/g as the calcination temperature raised from 400 to 500 and 600°C. The

decreased specific surface area could be attributed to the increase in LDH crystallite size at higher calcination temperature.

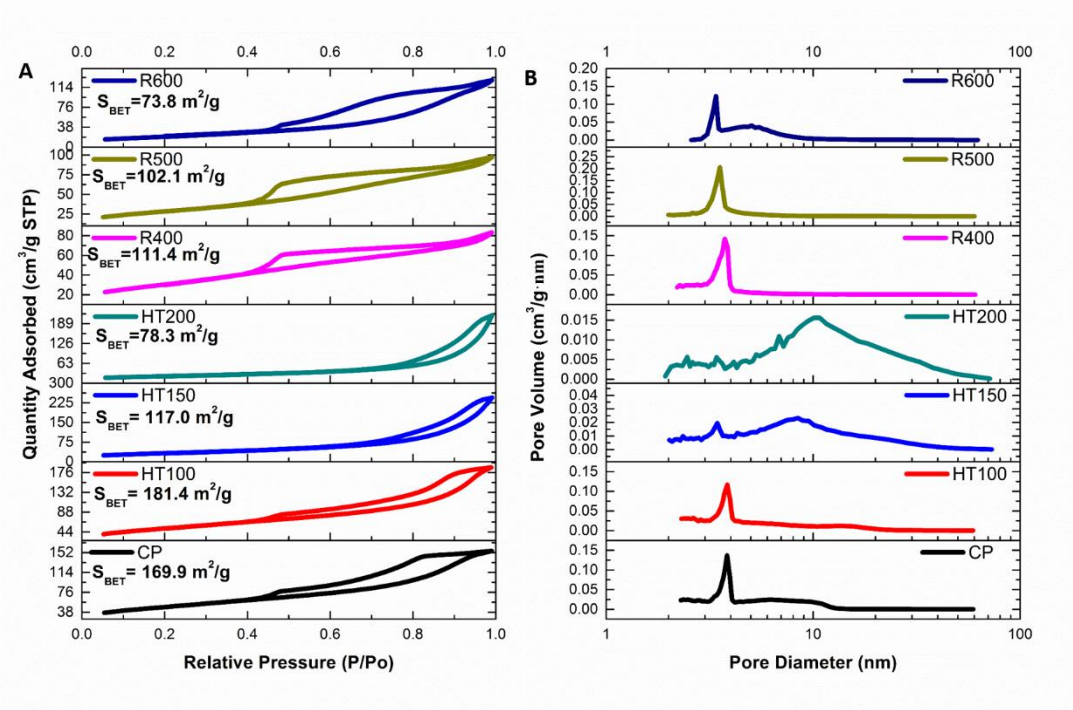

Figure 15 N_2 adsorption-desorption isotherms (A) and Pore size distribution (B)

Pore size distribution of the samples **Figure 15B** were plotted using BJH desorption data. Average pore size and pore volume were summarized in Table 4. For the pristine CP sample, two peaks at 3.8 and 6.3 nm were observed, which was consistent with the values in the literature.[106] Hydrothermal treatment at 100°C did not change the pore size distribution significantly, although the second peak was slightly broadened. When the hydrothermal temperature was raised to 150 and 200°C, the first peaks shrank significantly and the second peaks grew and shifted to 8.4 and 10.8 nm respectively. The average pore size for HT150 and HT200 was 10.8 and 14.3 nm, larger than that of 6.3 and 5.5 nm for

the HT100 and CP samples. This increase in pore size could be the result of increased LDHs flake size due to hydrothermal treatment. Reconstructed samples had similar pore size distribution with the pristine CP sample. R400 and R500 had only the sharp peaks at 3.7 and 3.5 nm while the R600 sample had two peaks at 3.4 and 5 nm. Average pore sizes were 4.2, 4.4 and 5.7 nm for R400, R500 and R600 respectively. The increasing trend with temperature in pore size agreed well with the flake size changes observed in SEM analyses.

3.3.4 Optical Property and CO_2 Adsorption Capability

Band gaps of the samples measured from UV-Vis absorption spectra are listed in **Table 5**. The CP sample had a band gap of 3.40 eV, in consistent with the reported value for amorphous TiO_2.[108] Hydrothermal treatment at 100 °C (HT100) did not change the band gap. But when the hydrothermal temperatures were raised to 150°C and 200°C, the band gaps were slightly narrowed down to 3.32 and 3.31 eV, which could be attributed to the presence of anatase TiO_2 in the two samples. Band gaps of reconstructed samples were determined to be 3.42, 3.35 and 3.30 eV at calcination temperatures of 400, 500 and 600°C. The results indicate that all the treatments did not significantly change the band gap of the MgAlTi-LDH materials.

CO_2 adsorption capacities were measured from CO_2 isotherms obtained by the TGA instrument and shown in Table 5. The CP sample had a CO_2 adsorption capacity of 2.07 wt% or 0.47 mmol/g, the highest among all samples tested. The decrease in CO_2 adsorption capacity for the HT150, HT200, R400, and R600 was probably caused by the decreased surface area after hydrothermal and reconstruction treatment. All MgAlTi-

LDHs have a much higher CO_2 adsorption capacity than commercial TiO_2-P25 nanoparticles, which is a mixture of anatase and rutile crystal phases[109].

Table 5 Optical and CO_2 adsorption parameters of MgAl-Ti-LDHs

Sample	CP	HT100	HT150	HT200	R400	R500	R600	P25
Band gap (eV)	3.40	3.40	3.32	3.31	3.42	3.35	3.30	3.20
CO_2 adsorption capacity (wt%)	2.07	N/M*	0.66	0.62	0.85	N/M*	0.59	0.11
CO_2 adsorption capacity (mmol/g)	0.470	N/M*	0.150	0.141	0.193	N/M*	0.134	0.025
CO_2 adsorption capacity per unit surface area (μmol/m^2)	2.77	N/M*	1.28	1.80	1.73	N/M*	1.82	0.5

*N/M: not measured

3.3.5 Photocatalytic Activity for CO_2 Photoreduction with H_2O

The photocatalytic activity of MgAlTi-LDHs were tested for CO_2 photoreduction by UV light irradiation for 5 h with continuous moisturized CO_2 feeding. Baseline experiments were first carried out in the dark with the photocatalyst or in the absence of photocatalyst under light irradiation, and CO_2 reduction products were observed. Under light irradiation in the presence of photocatalyst, CO was identified as the major product with only trace amount of CH_4 detected, which was consistent with our previous reports on TiO_2 based photocatalysts for CO_2 reduction [2].

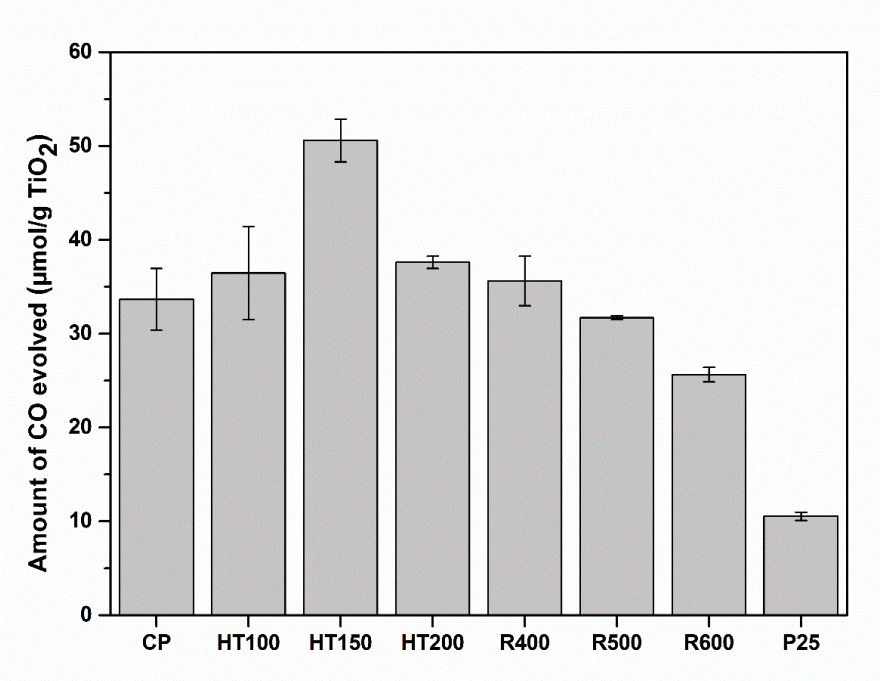

Figure 16 Amount of CO (normalized by catalyst mass) evolved by CO_2 photoreduction with water vapor during 5 h UV irradiation.

The amounts of CO production evolved within 5 h with moisturized CO_2 feeding were compared for all the MgAlTi-LDHs samples and commercial TiO_2-P25 nanopowders. The experiments were repeated two to three times for each material and the results (average and deviation) of CO production per unit gram of active photocatalyst material (TiO_2) are shown in **Figure 16**. P25 had the lowest CO production at around 10 μmol/g. The CP sample, with amorphous TiO_2, produced 33 μmol/g CO, more than two times of that by P25. This result indicates that amorphous TiO_2 in MgAlTi-LDH is photocatalytically active. The much higher activity of CP than that of P25 is likely due to the much large surface area (BET specific area of CP and P25 are 169.9 and 50 m^2/g, respectively) and thus better dispersion of Ti species, as well as the facilitated CO_2

adsorption capacity due to the MgAl-LDH. All the hydrothermal treated (HT) samples showed enhanced photoactivity compared to the CP sample. HT150 showed the highest CO production at around 50 μmol/g, 50% higher than that of the CP sample and four times higher than that of P25. Either lower (100 °C) or higher (200 °C) hydrothermal temperature did not improve photocatalytic activity significantly compared with the CP sample. For the reconstructed samples, however, only R400 showed slightly increased CO production, while the R500 and R600 showed rather decreased CO production compared with the CP sample. Nevertheless, they all had photocatalytic activities higher than P25.

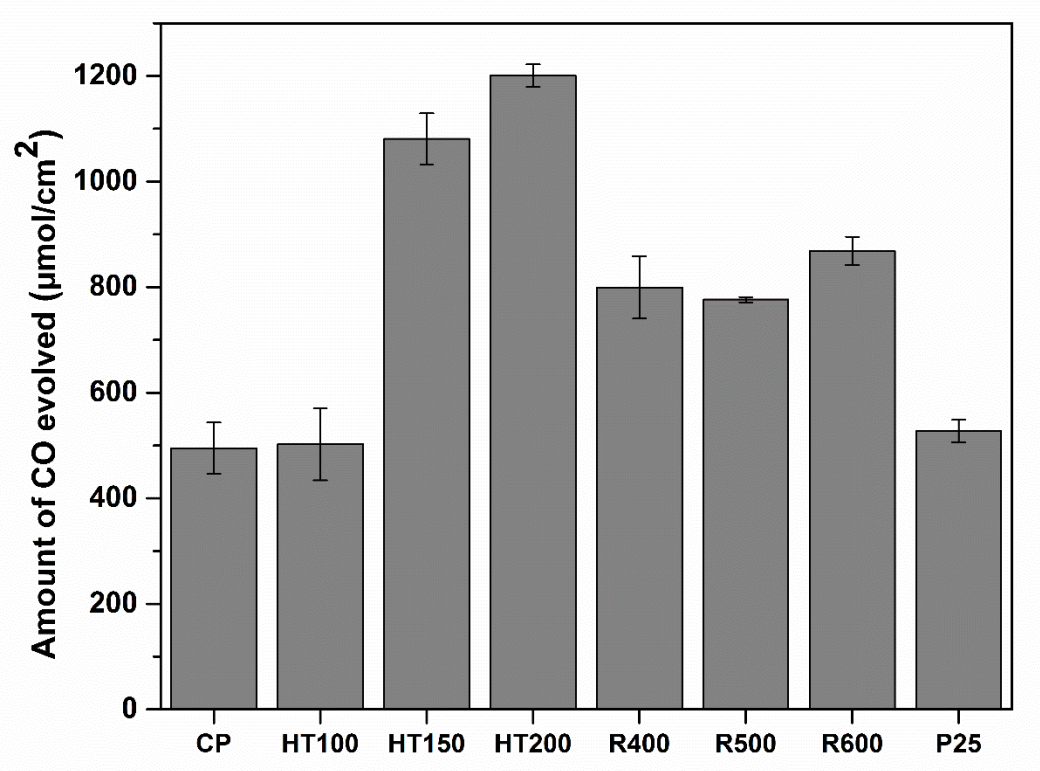

Figure 17 Amount of CO (normalized by catalyst surface area) evolved by CO_2 photoreduction with water vapor during 5 h UV irradiation

The results of CO production by the various catalysts were also normalized by surface area and compared in **Figure 17**, which further demonstrated the better performance of hydrothermally treated sample over those prepared by calcination-reconstruction method. The CO_2 adsorption capability normalized by surface area was also added in **Table 5**. HT200 had the highest CO production per unit surface area and was twice as high as those of CP and P25 samples. Even though HT200 and R600 had similar CO_2 adsorption capacity per unit surface area, the photoactivity of HT200 was greater than that of R600. Since HT200 and R600 had similar band gap energies, a possible reason is that HT200 had a smaller anatase crystallite size (12.3 nm) than R600 (30.1 nm), which resulted in more number of surface active sites. However, HT150 had the smallest anatase crystallite size (8.4 nm), but the surface area normalized photoactivity of HT150 was slightly less than that of HT 200. This maybe because the CO_2 adsorption capacity of HT150 per unit surface area was lower and its band gap was slightly larger than HT200. The above results suggest there exists an optimal anatase crystallite size for CO_2 photoreduction, due to the balance between band gap and surface active sites of TiO_2 particles.[110,111]

By correlating **Figure 16** and **Figure 17** with the materials properties, it can be concluded that the materials properties that may affect the CO_2 photoreduction activities include TiO_2 crystallinity and crystallite size, band gap, surface area, and CO_2 adsorption ability. Among all the samples tested, the two samples HT150 and HT200 showed the highest overall CO production. HT150 was the most active catalyst when normalized by mass and HT200 was the most active one when normalized by surface area. It is likely the

combination of the following properties made them superior catalysts to others: (1) their band gaps were among the smallest (3.31-3.32 eV), (2) HT150 had a relatively high surface area (117.0 m^2/g), (3) both had crystalized anatase TiO_2 with small crystallite size (8.4 and 12.3 nm for HT150 and HT200, respectively), and (4) the LDH composition and structure enhanced their CO_2 adsorption capacities. Although R600 also had anatase TiO_2 nanocrystals and relatively small band gap, its relatively large crystallite size (30.1 nm) and low surface area (74 m^2/g) prevented improvement in the overall photocatalytic activity. However, the general higher activity of all MgAlTi-LDH materials than P25 suggests the advantages of this type of new photocatalyst materials because of their better TiO_2 dispersion and higher CO_2 adsorption capacity.

3.4 Conclusions

In this study, a new series of photocatalysts, MgAlTi-LDHs, with different materials structures have been fabricated and demonstrated for CO_2 photoreduction with water vapor to produce CO. The MgAlTi(CP) sample prepared by a coprecipitation method had amorphous TiO_2 species but was fairly active and had much higher photoactivity than the commercial TiO_2-P25. Hydrothermal treatment at 150-200°C converted the amorphous Ti species in the LDHs to anatase nanocrystals while maintaining the characteristic LDH structures. The optimum hydrothermal temperature was identified to be in the range of 150 to 200 °C (corresponding to photocatalysts HT150 and HT200). HT150 was four times more active than P25 and 50% more active than the CP sample, when normalized by catalyst mass. HT150 was four times more active than P25 and 50% more active than the CP sample, when normalized by catalyst mass. The

activity of HT200 was twice as high as those of CP and P25, when normalized by catalyst surface area. Alternatively, reconstructing the CP sample at a calcination temperature of 600°C resulted in crystal anatase TiO_2, but the larger anatase crystallite size and relatively low surface area of R600 made its catalytic activity inferior to the HT150 and HT200 samples. In general, distributed crystalline TiO_2 in LDHs has better photocatalytic activity than amorphous TiO_2 for CO_2 photoreduction with H_2O. Band gap, specific surface area, and TiO_2 crystallinity and crystallite size are all important factors affecting the photocatalytic activity, and the enhanced CO_2 adsorption capacity introduced by the MgAl-LDH is particularly beneficial to CO_2 photoreduction. The discovery of this new type of MgAlTi-LDH (HT) material is important in the development of efficient CO_2 reduction photocatalysts.

4. ENHANCING PHOTOCATALYTIC CO_2 REDUCTION BY COATING AN ULTRATHIN Al_2O_3 LAYER ON OXYGEN DEFICIENT TiO_2 NANORODS THROUGH ATOMIC LAYER DEPOSITION[4]

4.1 Introduction

Among anatase, brookite and rutile, anatase is the most studied TiO_2 crystal phase because it is easier to synthesis compared to brookite and more active compared to rutile. A basic anatase crystal formed naturally has a truncated bipyramidal structure usually enclosed by eight {101} facets and two {001} facets, and because the surface energy of {001} is greater than {101}, the exposed facet of anatase is dominated by {101} at 94%.[112] Recently, anatase nanomaterials with well-defined exposed facets {101}, {001} or {100} have been successfully prepared and investigated for the facet-dependent photoactivity of TiO_2. The effect of exposed facet attracted more attention. The promising results of combining the advantages of active facets and defect effects in our previous work[37] have inspired on the design of novel TiO_2 material with high percentage {100} facets exposed and high density of surface oxygen vacancies. To further improve the photocatalytic activity of TiO_2, ALD was used in this work to coat a layer of Al_2O_3 on the surface of TiO_2. The thickness of Al_2O_3 layer deposited on TiO_2 was controlled by ALD. The mechanism of the enhanced photocatalytic activity was proposed based on the materials characterization and activity test results. We have found that when the layer of Al_2O_3 was

[4]Part of this chapter is reprinted with permission from "Enhancing photocatalytic CO_2 reduction by coating an ultrathin Al_2O_3 layer on oxygen deficient TiO_2 nanorods through atomic layer deposition" by Huilei Zhao, Jiatang Chen, Guiying Rao, Wei Deng and Ying Li, 2017. *Applied Surface Science*, 404, 49-56, Copyright [2017] by Elsevier B.V.

very thin, the surface passivation ability of Al_2O_3 over TiO_2 could enhance the photocatalytic activity, but a thick layer of Al_2O_3 as an insulator could hinder the electron transfer to the surface, thus lowering the rate of CO_2 photocatalytic conversion.

4.2 Material and Methods

4.2.1 Material Preparation

Anatase nanorods (ANR) were prepared by a two-step hydrothermal method. Firstly, TiO_2 P25 (Evonik) was dispersed into a 10M NaOH solution, sealed in a Teflon-lined autoclave, and heated in an electric furnace at 140°C for 24 h to produce sodium titanates. The products were washed and centrifuged several times with D/I water till pH 10. Next, 2 g sodium titanates were mixed with D/I water and subject to a second hydrothermal process at 200 °C for 12 h. The resulting solids were separated from the liquid by centrifuge and washed with D/I water till pH 7. The anatase nanorods were obtained after drying the sample at 60 °C for 12 h.

The reduced anatase nanorods (ReANR) were prepared by mixing the ANR with $NaBH_4$ (1:1) in a mortar, and thermally treated in Ar at 300 °C for 30 min. The resulting mixed solids were washed with D/I water and centrifuged till pH 7. The ReANR was obtained after drying in the oven at 60 °C for 12 h. For comparison, pure anatase nanoparticles (ANP) were prepared by a simple hydrothermal method reported in our precious work.[113] Briefly, titanium (IV) bis(ammonium lactato) dihydroxyde (TALH) was mixed with 0.1 M urea, and hydrothermally treated at 160 °C for 24 h. The sample was washed and dried using the same method as in the procedure for ANR. The ANP was

finally calcined at 450 °C for 2 h to remove any possible organic residuals on the surface. The reduced ANP (ReANP) was also prepared using the same method as ReANR.

To obtain ALD coated Al_2O_3 on ReANR, a commercial ALD system (Savannah S200, Ultratech) was applied. For each coating process, ANR powders were loaded into a home-designed particle holder, which was placed in the middle of the reaction chamber of the ALD. To ensure adequate coating on porous materials, the ALD system was set in an "expo mode" assisted with a soft pump, which can prolong the time for precursor molecules to contact with the surface of ANR by slowing down the pressure decreasing rate. The pulse time of both the H_2O and Trimethylaluminum (TMA) was 0.03 s, and the reaction chamber was set at 200 °C. No external heater was applied to the TMA cylinder. The Al_2O_3 coated samples were denoted as xAl_ReANR, where x is the number of ALD cycles applied.

4.2.2 Material Characterization

X-ray diffraction (XRD, BRIKER D8) using Cu Kα irradiation at 45 kV and 40 mA diffracted beam monochromator was applied to detect the crystal structures of the photocatalyst samples. The surface morphology was obtained by scanning electron microscopy (SEM, JEOL JSM7500F) equipped with a cold cathode UHV field emission conical. The Energy-dispersive X-ray spectroscopy (EDS, Oxford) associated with SEM was used for surface elemental mapping and quantitative elemental composition analysis. Transmission electron microscopy (TEM) and high resolution-TEM (HR-TEM) taken by an FEI Tecnai G2 F20 ST instrument with 0.24 nm point and 0.15 nm information limitation at 200 keV was used to obtain the lattice structure of ANR and identify the

Al_2O_3 coating layer. UV−vis diffuse reflectance spectra were obtained by a Hitachi U4100 UV-Vis-NIR Spectrophotometer with Praying Mantis accessory. Photoluminescence (PTI QuantaMaster series Spectrofluorometer) was used to investigate the charge recombination emission using 360 nm incident light, scanning from 370 to 700 nm with scan rate 0.1nm/s. A 380 nm long pass filter was applied to the detector. X-ray photoelectron spectroscopy (XPS) was used to identify the chemical states of Ti, O and Al elements, using an Omicron XPS system using Omicron's DAR 400 dual Mg/Al X-ray source. All region and components were calibrated using C 1s peak at 284.8 eV.

4.2.3 Photocatalytic CO_2 Photoreduction

Photocatalytic activity test for CO_2 photoreduction with water vapor was performed in a cylindrical quartz tube reactor. For each activity test, 10 mg catalyst was dispersed on a piece of glass fiber filter paper. The filter paper was placed in the middle of the reactor, with the catalyst side facing the light irradiation direction. CO_2 (99.999%, Airgas) continuously passed through a water bubbler and brought the mixed CO_2 and H_2O gas (2.3vol% of H_2O) into the reactor. The reactor was first purged at 100 ml/min for 1 h to eliminate air and then maintained at 4 ml/min (continuous-flow mode) for the whole photoreaction process. A 450 W Xe lamp (Newport) was used as the UV-vis source. The light intensity is about 267.15 mW/cm2 in the range from 250 to 1050 nm, and 17.15 mW/cm2 in the UV range (<390 nm). The spectrum of the light source was shown in **Figure 18**. A 250 W infrared (IR) lamp was applied to keep the reactor at 100 °C, this is because a relatively higher reaction temperature can facilitate the desorption of the products and improve the activity of photo-activated TiO_2.[114] In addition, Slamet *et*

al.[115,116] reported elevated CO_2 photocatalytic conversion to CH_4 by increasing the reaction temperature to 100 °C. The effluent from the reactor was analyzed continuously by a gas chromatograph (GC, Fuel Cell GC-2014ATF, Shimadzu) equipped with a thermal conductivity detector (TCD) and a methanizer assisted flame ionization detector (FID).

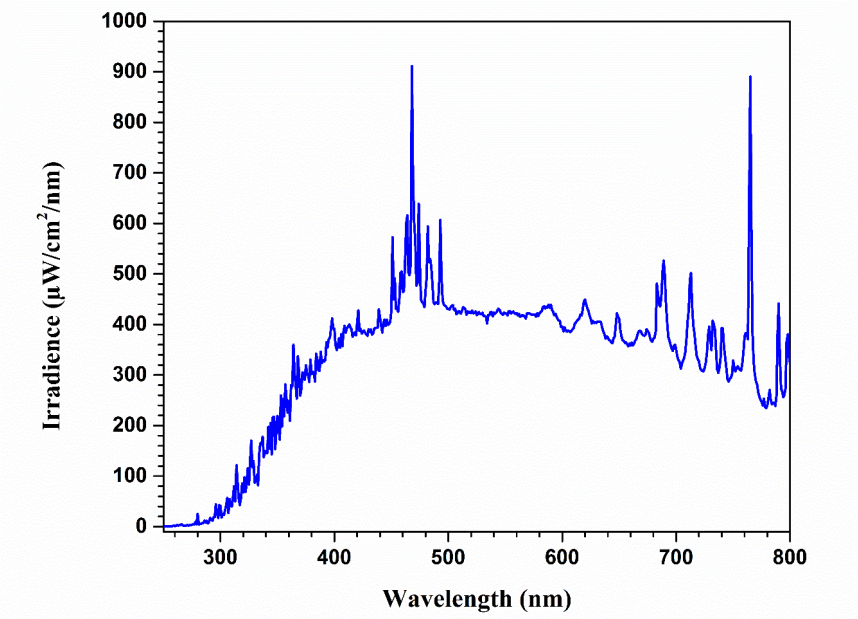

Figure 18 Irradiation spectrum of the Xe lamp used for CO_2 photoreduction experiments

4.3 Results and Discussion

4.3.1 Crystal Structure

The crystal structure of the materials synthesized was characterized by XRD. **Figure 19** shows the XRD patterns of the ReANR and 200Al_ReANR, both of which show characteristic peaks for anatase TiO_2 (tetragonal, space group I41/amd, JCPDS 21-1272). Peaks at 25.3, 37.1, 37.8, 38.9, 48.0, 53.9, and 55.0 degree can be assigned to (101), (103), (004). (112), (200), (105), and (211) crystal plane of anatase TiO_2, respectively. The full width at half maximum (FWHM) for peaks at 25.3, 37.8, and 48.0° was calculated

to be 0.011, 0.006, and 0.012, which are indexed to crystal planes (101), (004) and (200), respectively. Compared with the FWHM of anatase nanocuboids (0.11, 0.26, 0.09) with 95% {100} exposed facet reported in the literature, the ANR synthesized in this work with much smaller FWHM had better crystallinity. The peak intensity ratio I(101): I(004): I(200) was 100:14:40, while the standard ratio of anatase is 100:18:23, suggesting that the preferential crystallographic orientation of anatase nanorod synthesized was along [100] direction. For ALD coated catalyst, there was a very broad peak at 20-50°, observed from the intensity difference between ReANR and 200Al_ReANR (inset of **Figure 19**). The broad peak matched the amorphous Al_2O_3 by ALD reported in the literature,[117] indicating the successful coating of amorphous Al_2O_3 layer on nanorods.

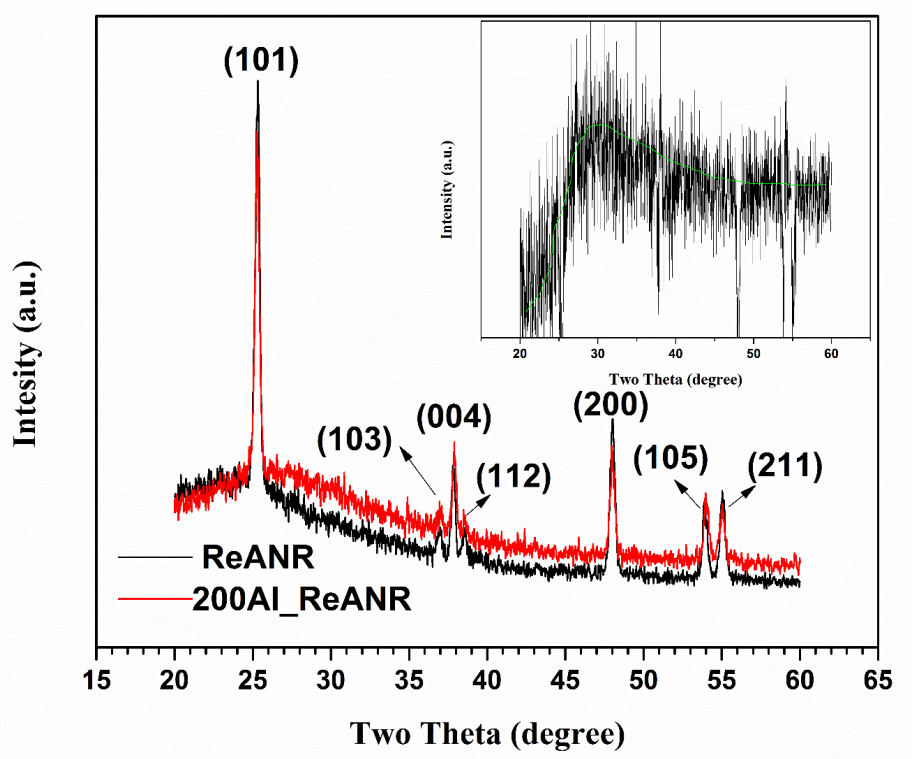

Figure 19 XRD patterns of ReANR and 200Al_ReANR
(Inset figure is intensity by subtracting intensity of ReANR from 200Al_ReANR)

4.3.2 Morphology

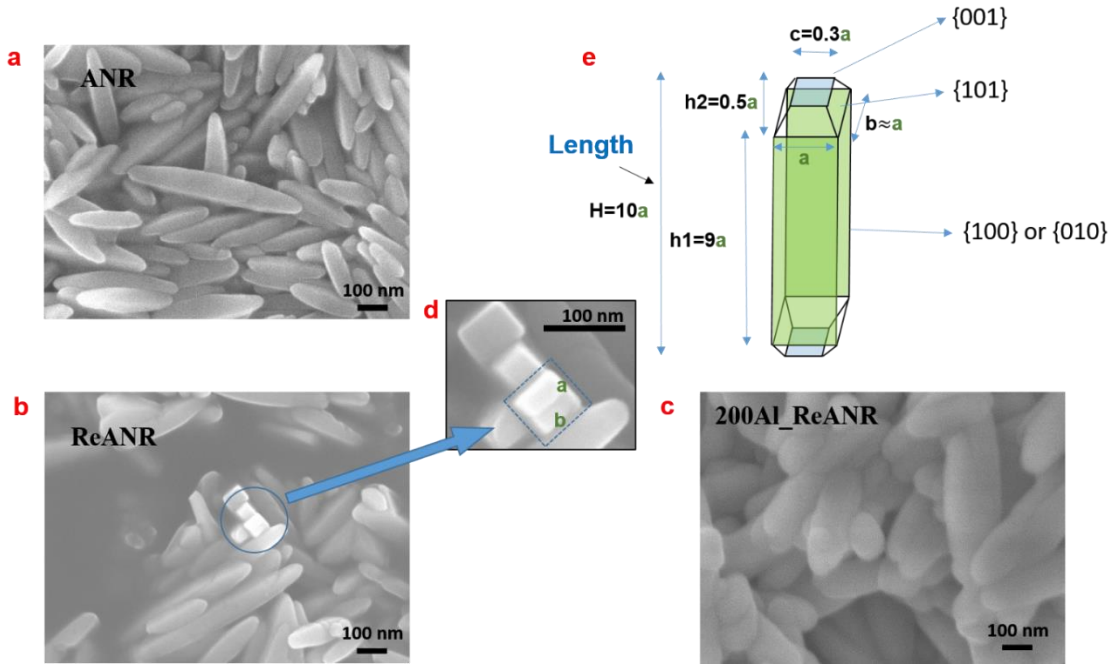

Figure 20 SEM images of ANR (a), ReANR (b), 200Al_ReANR (c), the enlarged image of the circled area (d), and the simulated geometry model of ANR (e)

The morphology of the photocatalysts was charcaterized by SEM in **Figure 20**. The rod-shape ANR (**Figure 20a**) and ReANR (**Figure 20b**) have well-defined lateral facets with sharp edges, and the adjacent parallel facets {100} and {010} are perpendicular as boxed off in **Figure 20d**. The rectangular shape has a width *a* of ~53 nm, and a depth *b* of ~58 nm, suggesting *a* is approximately equal to *b*. Thus, a geometry model of the ANR can be built based on the measurement in SEM, TEM, and HRTEM images, as shown in **Figure 20e**. The exposed facets of ANR were composed by four {100}/{010} facets as the lateral planes, two {001}as the end planes, and four {101} facet as the connecting planes. Although the anatase nanorods exhibited different lengths (along [001] direction), the aspect ratios of the rods are similar. The model parameters are estimated to

be a:b:c:H:h_1:h_2 = 1:1:0.3:10:9:0.5. The percentage of {100} facets exposed was calculated to be 91.5% using the method described in our previous work.[37] As shown in **Figure 20c**, after ALD coating of Al_2O_3 for 200 cycles on the surface of TiO_2, the size of the nanorods became larger, and the edges became blurry, suggesting the successful coating of Al_2O_3 on ANR.

4.3.3 Lattice Structure of ANR and Identification of Al_2O_3 Coating Layer

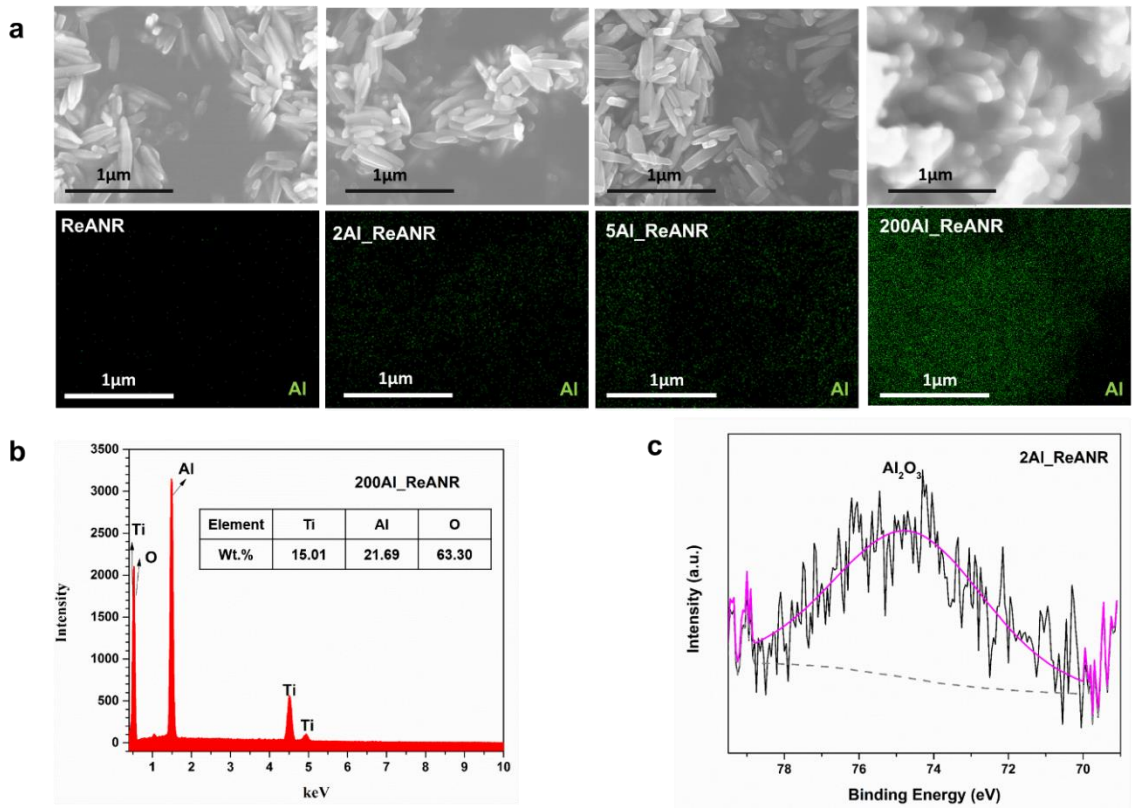

Figure 21 EDS mapping images of ReANR with different cycles of ALD Al_2O_3 coating (a), and the EDS elemental analysis spectrum of 200Al_ReANR (b), and the XPS for 2Al_ReANR (c)

The EDS mapping images and elemental analysis spectrum in **Figure 21** further confirm the existence of the Al_2O_3 layer. In **Figure 21a**, as the ALD cycle increased from

2 to 200, the size of nanorods increased. Moreover, the number of the green dots, which were corresponding to Al element, also increased with the increasing ALD cycle number. The surface quantitative elemental composition analysis (**Figure 21b**) shows an even higher concentration of Al (21.69 wt.%) than Ti (15.01 wt.%) on 200Al_ReANR. All the above results demonstrate the successfully coating of an ALD layer of Al_2O_3 whose thickness increases with an increasing ALD cycle number. For the sample 2Al_ReANR, the presence of the ultrathin layer of Al_2O_3 was also demonstrated by XPS results in **Figure 21c**. The broad peak at 74.75 eV represents typical characteristic of Al 2P (oxide).

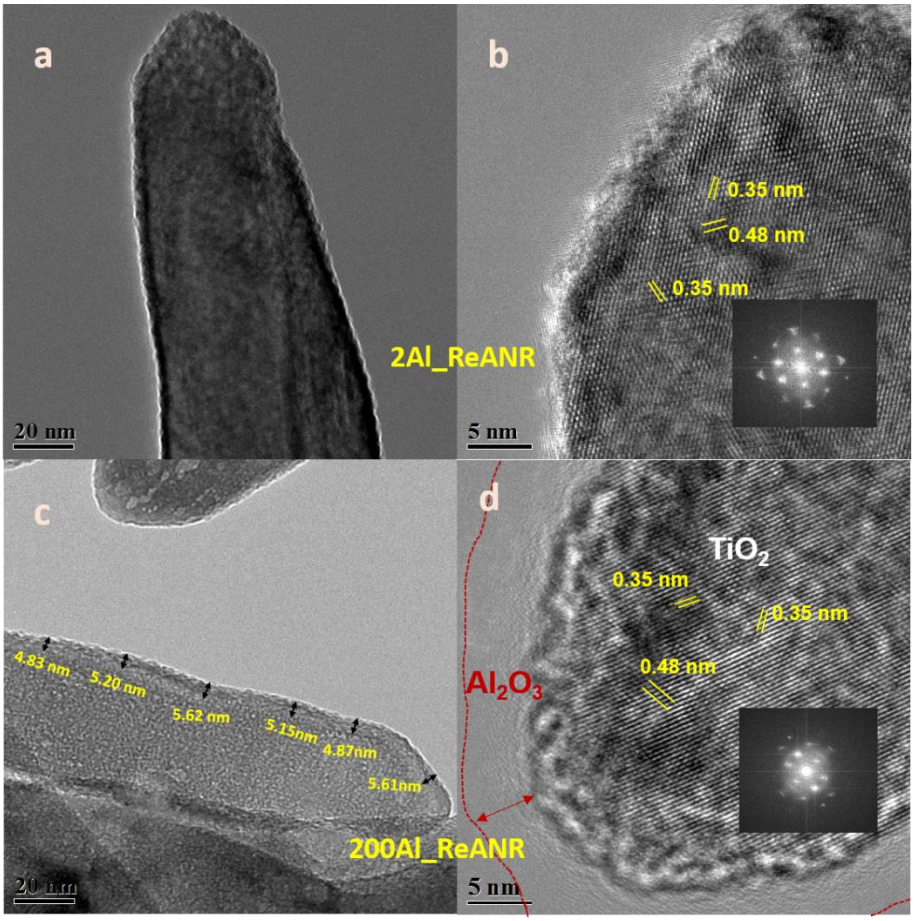

Figure 22 TEM and /HRTEM images of 2Al_ReANR (a and b) and 200Al_ReANR (c and d)

TEM and HRTEM were applied to obtain crystal structure information and verify the surface Al_2O_3 coating layer. Figure 22 compares the morphology of 2Al_ReANR and 200Al_ReANR. The rod-shaped structure shown in Figure 22**a** and **Figure 22c** agrees well with the SEM observation and literature report[32,35,36]. The lattice spaces of TiO_2 are measured to be 0.48, 0.35, and 0.35 nm in Figure 22**b** and Figure 22**d** based on the inset fast Fourier transform (FFT) images, corresponding to the (002), (101), and $(10\bar{1})$ facets, respectively.[118,119] For 2Al_ReANR in Figure 22**b**, the fuzzy edges may be attributed to the ultra thin layer of Al_2O_3 on the surface of TiO_2. The amorphous layer of Al_2O_3, which is outlined by dashed lines, can be observed clearly in **Figure 22d**. The amorphous Al_2O_3 gave the circle signal in the inset FFT image (Figure 22**d**). The thickness of the Al_2O_3 from the edges of the nanorod to the dashed lines was estimated to be 5 nm for the 200Al_ReANR sample, which also matches the average thickness measured in **Figure 22c**. Therefore, the growth rate of the Al_2O_3 overlayers estimated to be ~0.25 Å per cycle.

4.3.4 Optical and Charge Transfer Properties

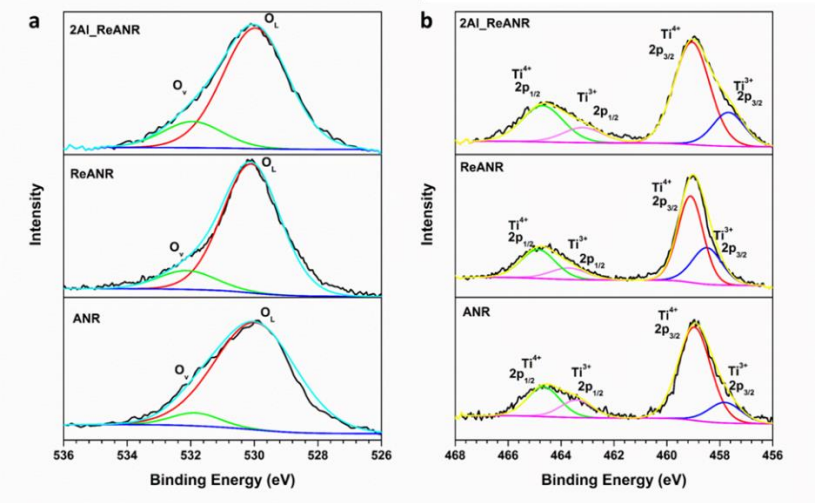

Figure 23 XPS O 1s spectra (a) and Ti 2p spectra of ANR, ReANR and 2Al_ReANR

Table 6 Binding energy values of O 1s, Ti 2p for ANR, ReANR and 2Al_ReANR

Sample	O 1s		Ti 2p1/2		Ti 2p3/2		Fraction of Ti^{3+}/Ti^{4+}
	O_V (eV)	O_L (eV)	Ti^{4+} (eV)	Ti^{3+} (eV)	Ti^{4+} (eV)	Ti^{3+} (eV)	
ANR	531.9	530.1	464.7	463.3	459.0	457.8	0.35
ReANR	532.2	530.1	464.9	463.7	459.1	458.5	0.48
2Al_ReANR	531.9	530.1	464.7	463.2	459.1	457.7	0.33

Based on the UV-vis absorption result (**Figure 24a**) and the Tauc plot (**Figure 24b**), the band gap of ANR was calculated to be 3.12 eV, while ReANR had a slightly reduced band gap, 3.04 eV. This agrees with the color change from white to grey after the reduction treatment by $NaBH_4$, due to the formation of V_O, which was confirmed by XPS shown in Figure 23.[120] According to the O 1s XPS spectra in **Figure 23a**, the oxygen vacancy peak (~532.0 eV) of ReANR and 2Al_ReANR was higher than that of ANR, suggesting more oxygen vacancies were formed after reduction.[121,122] Also, quantitative analysis of Ti^{3+} is given in **Table 6** in terms of the Ti^{3+}/Ti^{4+} fraction. It was found that after reduction, the Ti^{3+}/Ti^{4+} fraction increased from 0.35 (ANR) to 0.48 (ReANR). The increased formation of Ti^{3+} is another evidence of Vo formation.[123] With 2 cycles of Al_2O_3 ALD coating, the band gap was slightly increased to 3.08 eV, compared to uncoated ANR, which may be because the surface Vo were partially consumed by H_2O during the ALD pulsing process.

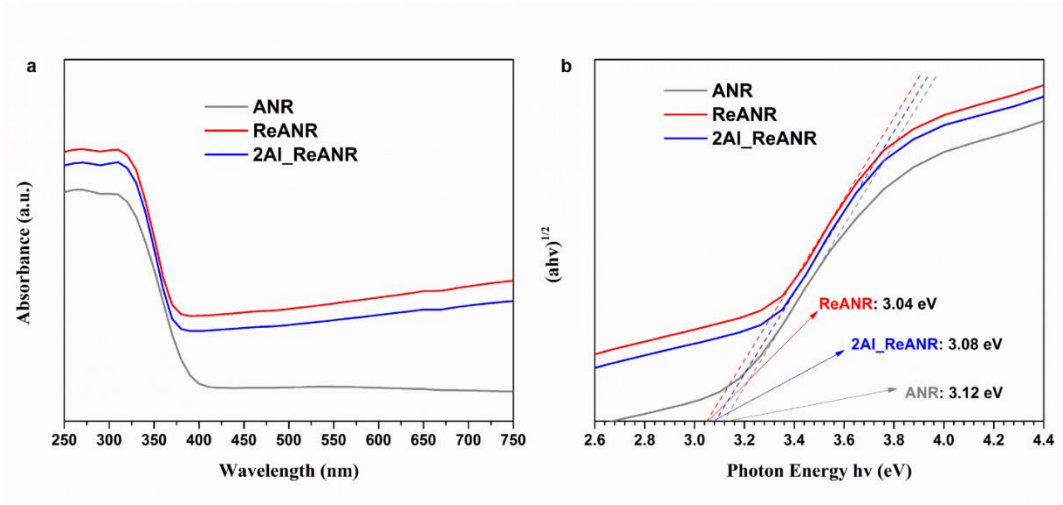

Figure 24 UV-vis absorption spectra (a) and band gap measurement using Tauc plot (b)

The charge recombination property of the phtoocatalysts was characterized by photoluminescence. Promoted charge separation lowering the rate of radiative or non-radiative recombination leads to the quenching of the photoluminesces intensity.[124] According to the photoluminescence results (**Figure 25**), the reduced sample ReANR had a much lower intensity of emission peak around 550 nm than ANR, suggesting a reduced charge recombination on ReANR. This is likely because the ReANR had more surface V_O, which can generate donor states below the conduction band (CB), promoting the charge separation and transportation.[125] After the surface of ReANR was coated with 2 or 200 cycles of Al_2O_3 ALD, the height of the 550 nm emission peak of 2Al_ReANR and 200Al_ReANR was further lowered, indicating the coated overlayer further helped to suppress the surface charge recombination. The photoluminesces intensities of 2Al_ReANR and 200Al_ReANR were quite close to each other, indicating the ultrathin layer of Al_2O_3 coating in the range from 0.5 Å to 5 nm was capable to promote the charge

separation. This is consistent with existing literature reports that the thickness of Al_2O_3 for the surface passivation effect varies from several tenths of Å to tens of nm.[126-128]

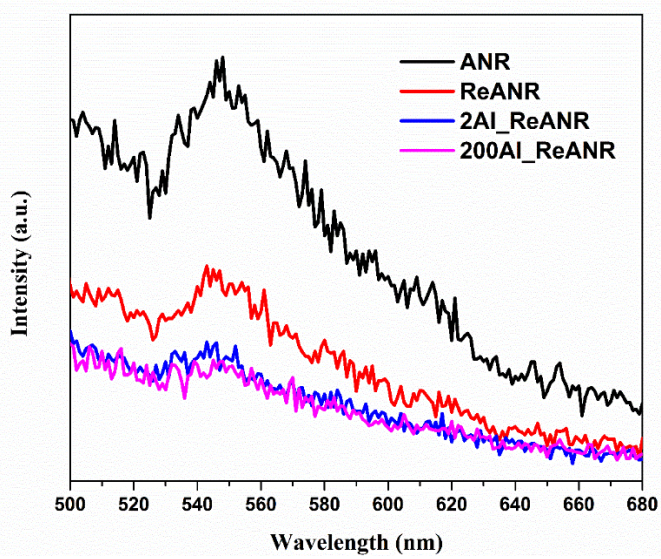

Figure 25 Photoluminescence spectra of anatase nanorod photocatalysts

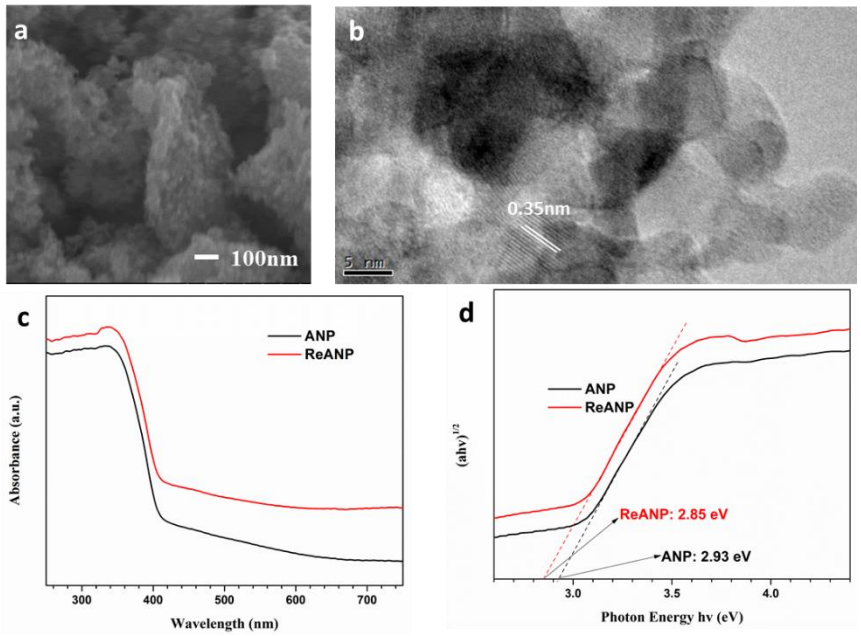

Figure 26 SEM (a) and HRTEM (b) of ANP, UV-vis spectra (c) and bandgap measurement using Tauc plot (d) of ANP and ReANP

The morphology, crystal structure, and optical property characterization results of anatase nanoparticles (ANP) are shown in Figure 26. The reduction process did not change the morphology and the crystal structure of ANP, thus only SEM and TEM images of ANP were shown. The SEM image in Figure 26**a** shows the fine nanoparticle morphology of the ANP, which resulting in the high surface area of ANP. The HRTEM image in **Figure 26b** shows the lattice space of ANP crystals is 0.35 nm, attributed to the most common {101} facet of anatase. The estimated band gap energies of ANP (2.95 eV) and ReANP (2.85 eV) (as seen in **Figure 26d-c**) are smaller than those of ANR (3.12 eV) and ReANR (3.04 eV).

4.3.5 Photocatalytic Activity for CO_2 Photoreduction with H_2O under UV-Vis Irradiation

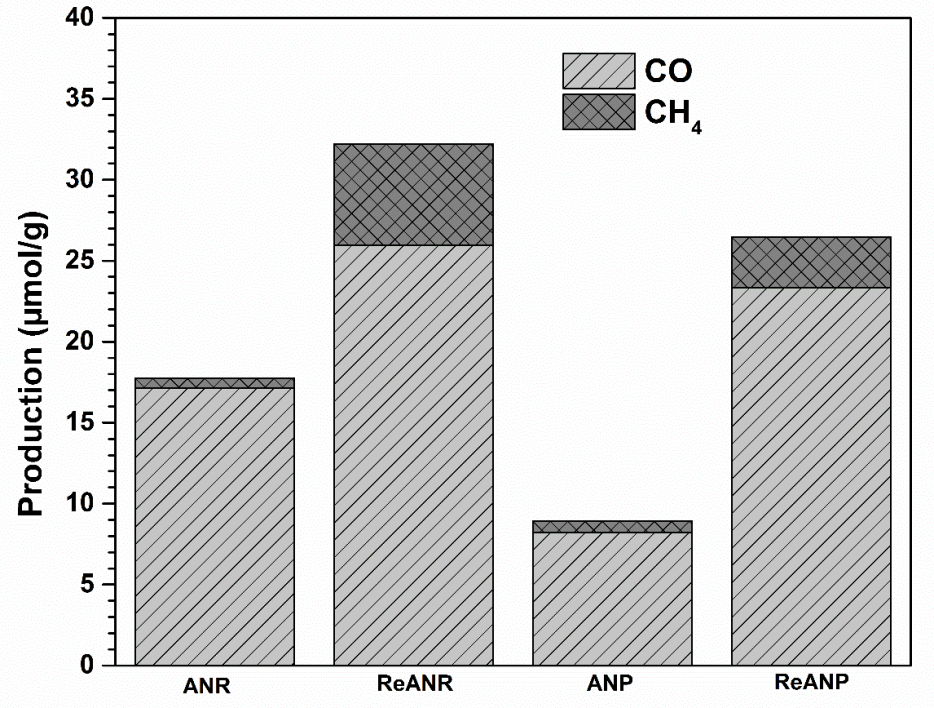

Figure 27 The production of CO and CH_4 during a 4 h UV-vis irradiation period by anatase nanorods and nanoparticles

The photocatalytic activity of the synthesized photocatalysts for CO_2 photoreduction was tested by UV-vis light irradiation for 4 h with continuous CO_2 and H_2O vapor feeding. Two control experiments were conducted: (1) in the dark with the photocatalyst, and (2) under light irradiation without photocatalyst. In both cases, no CO_2 reduction products were detected. Under light irradiation in the presence of photocatalysts, CO and CH_4 were detected as the major products of CO_2 photoreduction with H_2O.

The production of CO and CH_4 from CO_2 photoreduction with H_2O within 4 h was compared among ANR, ReANR, ANP and ReANP, as shown in Figure 27. As shown in Figure 26**a-b**, ANP has isotropic nanoparticle structure, and {101} as the dominating facet. Even though ANP had a lager surface area than ANR due to the much smaller particle size of ANP (5-10 nm, Figure 26**a-b**, which was also reported in our previous work[113]) than ANR (a few hundred nm in length as shown in **Figure 20**), ANP produced 50% less amount of CO (8.2 μmol/g) than ANR (17.1 μmol/g). There are two possible reasons for the higher CO production on ANR over ANP was because the following reasons. First, ANR has a very high percentage (91.5%) of exposed {100} facet that has 100% active Ti_{5C} sites; by contrast, ANP has zero percent {100} facet. Second, the anisotropic structure of ANR may also enhance charge separation between different facets. The reduced sample ReANR had 50% higher CO production and 10 times higher CH_4 production than ANR. The improvement by ReANR can be attributed to the enhanced light absorption and formation of surface oxygen vacancies. The light absorption of ReANR was enhanced as evidenced by the narrowed band gap of 3.04 eV, compared with 3.12 eV for ANR. In addition, ReANR prepared by reducing ANR with $NaBH_4$ had Vo

created on the surface rather than in the bulk.[129] The Vo in the bulk is believed to be recombination centers for electrons and holes,[130] whereas, Vo on the surface facilitates CO_2 adsorption and activation[42,43], and promote electron transfer. The promoted CH_4 production was attributed to the increased local electron density by Vo, since CH_4 formation involves 8 electrons, while only 2 electrons are required for CO formation. When comparing the activity of ReANR and ReANP, one can find that the production of both CO and CH_4 were higher by ReANR and the overall production of CO and CH_4 by ReANR was 22% higher than ReANP. The results reveal the superior photocatalytic activity of ReANR that takes the advantages of the active exposed facet and surface defect effects. However, it can also be noticed that the activity difference between nanoparticles and nanorods became smaller after reduction. It may be because ReANP may have more V_O formed than ReANR due to the high surface area of ReANP. In addition, the band gap of anatase nanoparticles was reduced from 2.95eV to 2.85eV after $NaBH_4$ reducing treatment (Figure 26c-d). The further narrowed band gap of ReANP compared to ReANR (3.04 eV) leads to higher light absorption capability of ReANP, which may be another reason for the less difference in activity between the reduced nanorods and nanoparticles.

The CO_2 photocatalytic reduction with H_2O was also conducted on Al_2O_3 coated ReANR with varied thickness of Al_2O_3 coating layer. **Figure 28** compares the CO and CH_4 production on ReANR with different cycles (0-200) of ALD coated Al_2O_3. By applying less than 5 cycles of ALD, the Al_2O_3 coated ReANR had enhanced overall ($CO+CH_4$) production than uncoated ReANR, with 2 cycles being the optimum, about 40% higher overall production (45.2 μmol/g in total with 40.8 μmol/g CO and 4.4 μmol/g

CH_4) than ReANR(32.1 μmol/g in total). A thin layer of Al_2O_3 deposited on the surface can passivate the trapping states caused by the surface oxygen vacancies, and consequently reduce the recombination of electrons and holes, as revealed by the photoluminesces results. The electrons can still reach to the surface by tunneling or other effects and react with the gas molecules to produce CO and CH_4 when the layer of Al_2O_3 coating is very thin. Due to the passivation effect of Al_2O_3, the surface recombination was suppressed, resulting in the enhanced CO production, and the increase of the overall electron involved. At the same time, the surface electron density was decreased, which can explain the decline of CH_4 selectivity.

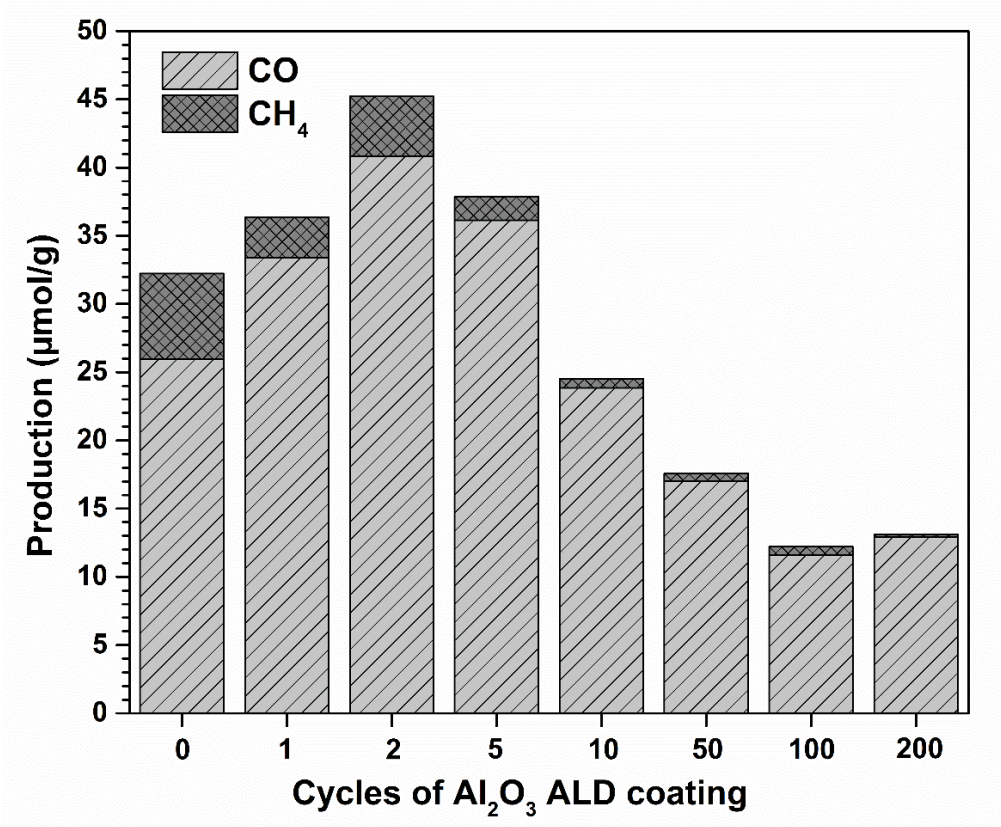

Figure 28 The production of CO and CH_4 during a 4 h UV-vis irradiation period by Al_2O_3 coated ReANR with different ALD cycles

However, both CO and CH_4 production decreased with increasing number of ALD cycles when more than 5 cycles were applied. When more than 100 cycles of ALD was applied, the overall production was reduced to ~12 μmol/g with negligible amount of CH_4. The insulating property of a thick layer of Al_2O_3may have decreased the surface electron density, which leads to an overall low product yield and low selectivity of CH_4. Future studies will continue to focus on the application of ALD on the design of innovative photocatalyst, and the effect of varied coating materials on the performance of TiO_2.

To confirm the catalyst was active under UV light, 2Al_ReANR was tested for CO_2 photoreduction with H_2O under UV irradiation (mercury lamp, UVP LLC, USA; λ= 365 nm, I= 13.12 mW/cm^2,). The production under UV irradiation was compared to that under UV-vis irradiation (450 W Xe lamp, Newport, USA; $I_{(\lambda<390\ nm)}$ =17.15 mW/cm^2, $I_{(390\ nm<\lambda<1050\ nm)}$ =250 mW/cm^2) in **Figure 29**. Note that although different light sources were used, the intensities of the UV portion from the two lights were close to each other. The production of CO and CH_4 in 4 h UV irradiation was 2.8, and 2.0 μmol/g, respectively, demonstrating the catalysts prepared in this work are photoactive for CO_2 photoreduction under UV only irradiation. While, under UV-vis irradiation, the production of CO (40.8 μmol/g) and CH_4 (4.4 μmol/g) was 14 and 2 times as much as those under UV only. The result suggests both UV and visible lights contributed to the production of CO and CH_4 production while the visible light activity was superb. Thus, catalysts with a smaller band gap, or higher visible light absorption capability may have higher photocatalytic activity for CO_2 photoreduction.

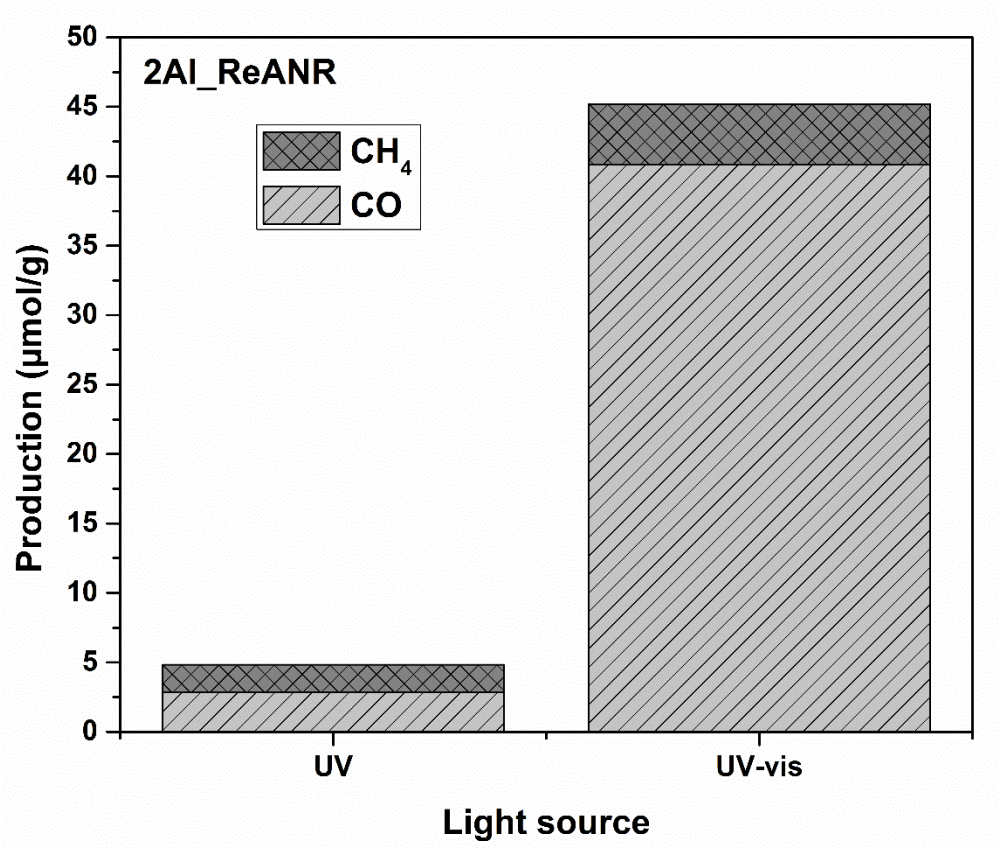

Figure 29 CO_2 photoreduction on 2Al_ReANR under UV only (from a mercury lamp) or UV-vis light irradiation (from a Xe lamp)

The stability of 2Al_ReANR, which has the optimal thickness of Al_2O_3 coating layer, was tested by 5 cycles (8 h/cycle) of activity tests. After each 8h cycle test, the photocatalysts were wetted by DI water and dried at 60 °C prior to the next cycle test. The cycling performance results are presented in in **Figure 30**. It shows the production rate of $CO+CH_4$ after 5 cycles maintained ~80% of the initial value, suggesting a relatively high stability of 2Al_ReANR. In addition, the color of ReANR and Al_2O_3 coated ReANR remained the same gray color for months, which also indicates the prepared materials are very stable.

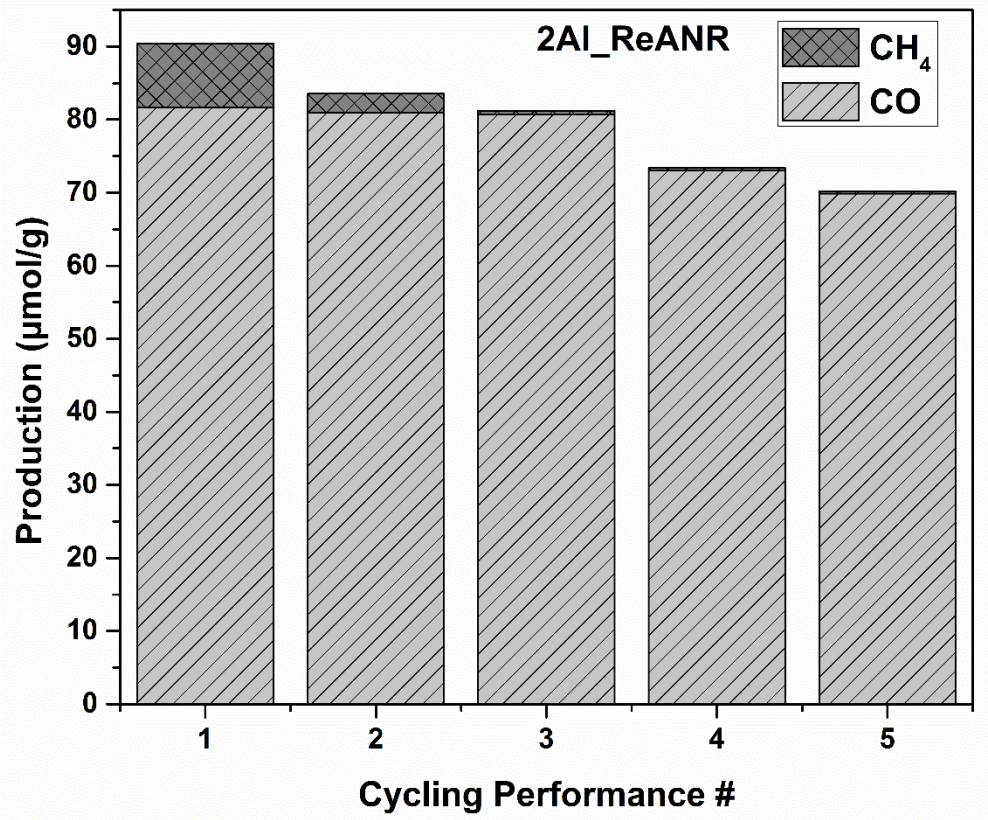

Figure 30 Cycling performance for CO_2 photoreduction with H_2O on 2Al_ReANR

4.4 Conclusions

Three materials innovations have been applied in this work to synthesize a unique nanostructured photocatalyst (TiO_2 anatase nanorods with over 90% exposed {100} facet, oxygen-difficient surface, and ALD coated Al_2O_3 overlayer), which demonstrated significantly enhanced capability for CO_2 photoreduciton with H_2O to produce CO and CH_4. ANR with dominating {100} facets, despite a smaller surface area, was much more active than ANP. Reduced ANR facilitated CO_2 adsorption and activation due to surface oxygen vacancies. However, the density of surface states increased with increasing oxygen vacancies, which may be detrimental to photocatalytic reactions. An ultrathin

overlayer of Al_2O_3 deposited by ALD demonstrated the ability to passivate the surface states of reduced ANR and thus further enhanced the yield of CO_2 photoreduction. The thickness of the Al_2O_3 coating is found to be critical to the photocatalytic performance of TiO_2. Two cycles of ALD coating or approxminately 0.5 Å Al_2O_3 corresponded to the optimum CO and CH_4 production. However, when more than five ALD cycles was applied, the CO and CH_4 production decreased, likely because the relatively thick overlayer inhibited electron transfer to the catalyst surface, although the surface passivation effect was still in effect. The strategy of ALD coating of a surface passivation layer can be applied to other photocatalysts beyond TiO_2 and other engineered surfaces and nanostructures, which may lead to the discovery of efficient, stable photocatalysts for CO_2 photoreduction with H_2O.

5. SUMMARY AND PROPOSED FUTURE WORK

The urgent need to reduce CO_2 emission and produce alternative energy raises the attention to advanced technologies of CO_2 utilization. Photocatalysts assisted CO_2 photoreduction is a very promising approach because it can convert CO_2 to value added products using photo energy. TiO_2 is the most extensively studied photocatalyst in this application but its catalytic performance is limited because of intrinsic materials properties such as large band gap and fast electron-hole recombination. This dissertation focuses on the innovative design of TiO_2 based nanomaterials for improve CO_2 photoreduction from the four direction (1) crystal structures, (2) CO_2 gas adsorption capability, (3) exposed facets and (4) defect property.

(1) The interfaces between anatase and brookite nanocrystals are believed to enhance photo-induced charge transfer and electron-hole separation

(2) New type of MgAlTi-LDH (HT) material, i.e. MgAl-LDHs with TiO_2 crystals showed higher CO_2 photoreduction because of the enhanced CO_2 adsorption capability.

(3) TiO_2 anatase crystals with active {100} facet exposed exhibited higher photocatalytic activity of CO_2 conversion compared to TiO_2 with {101} as the dominating facet.

(4) The photocatalytic activity of TiO_2 for CO_2 photoreduction was greatly improved by introducing surface defects. And a ultrathin layer of Al_2O_3 coating could further promote the photocatalytic performance due to the surface passivation effect of the coating layer.

Based on the current knowledge of design of TiO_2 based material and the research results, the future work was proposed in the following directions.

(1) Better under standing about the mechanism of the complicated reaction path of CO_2 photoreduction in gas adsorption, activation and reduction, and charge transfer.

(2) Investigate the defects effects on CO_2 photoreduction.

(3) Surface modification of photocatalyst using ALD technique

REFERENCES

(1) Dhakshinamoorthy, A.; Navalon, S.; Corma, A.; Garcia, H. *Energy & Environmental Science* **2012**, *5*, 9217-9233.

(2) Liu, L. J.; Zhao, H. L.; Andino, J. M.; Li, Y. *ACS Catalysis* **2012**, *2*, 1817-1828.

(3) Huang, J.; Liu, Y.; Lu, L.; Li, L. *Research on Chemical Intermediates* **2012**, *38*, 487-498.

(4) Zhao, C. Y.; Krall, A.; Zhao, H. L.; Zhang, Q. Y.; Li, Y. *Int. J. Hydrogen Energy* **2012**, *37*, 9967-9976.

(5) Izumi, Y. *Coordination Chemistry Reviews* **2013**, *257*, 171-186.

(6) Liu, L.; Li, Y. *Aerosol Air Qual. Res.* **2014**, *14*, 453-469.

(7) Ni, M.; Leung, M.; Leung, D.; Sumathy, K. *Renew. Sust. Energ. Rev.* **2007**, *11*, 401-425.

(8) Kumar, S.; Devi, L. *J. Phys. Chem. A* **2011**, *115*, 13211-13241.

(9) Habisreutinger, S.; Schmidt-Mende, L.; Stolarczyk, J. *Angew Chem. Int. Ed. Engl.* **2013**, *52*, 7372-7408.

(10) Yang, X.; Salzmann, C.; Shi, H.; Wang, H.; Green, M.; Xiao, T. *J. Phys. Chem. A* **2008**, *112*, 10784-10789.

(11) Inoue, T.; Fujishima, A.; Konishi, S.; Honda, K. *Nature* **1979**, *277*, 637-638.

(12) Yahaya, A.; Gondal, M.; Hameed, A. *Chem. Phys. Lett.* **2004**, *400*, 206-212.

(13) Zhu, Q.; Qian, J. S.; Pan, H.; Tu, L.; Zhou, X. F. *Nanotechnology* **2011**, *22*.

(14) Reyes-Coronado, D.; Rodriguez-Gattorno, G.; Espinosa-Pesqueira, M. E.; Cab, C.; de Coss, R.; Oskam, G. *Nanotechnology* **2008**, *19*.

(15) Landmann, M.; Rauls, E.; Schmidt, W. G. *J Phys-Condens Mat* **2012**, *24*.

(16) Liao, Y. L.; Que, W. X.; Jia, Q. Y.; He, Y. C.; Zhang, J.; Zhong, P. *Journal of Materials Chemistry* **2012**, *22*, 7937-7944.

(17) Ozawa, T.; Iwasaki, M.; Tada, H.; Akita, T.; Tanaka, K.; Ito, S. *J Colloid Interface Sci* **2005**, *281*, 510-513.

(18) Liu, G.; Wang, X. W.; Chen, Z. G.; Cheng, H. M.; Lu, G. Q. *J Colloid Interface Sci* **2009**, *329*, 331-338.

(19) Carneiro, J. T.; Savenije, T. J.; Moulijn, J. A.; Mul, G. *Journal of Physical Chemistry C* **2011**, *115*, 2211-2217.

(20) Hurum, D. C.; Agrios, A. G.; Crist, S. E.; Gray, K. A.; Rajh, T.; Thurnauer, M. C. *J. Electron Spectrosc. Relat. Phenom.* **2006**, *150*, 155-163.

(21) Stengl, V.; Kralova, D. *Mater Chem Phys* **2011**, *129*, 794-801.

(22) Deng, Q. X.; Wei, M. D.; Hong, Z. S.; Ding, X. K.; Jiang, L. L.; Wei, K. M. *Curr Nanosci* **2010**, *6*, 479-482.

(23) Dambournet, D.; Belharouak, I.; Amine, K. *Chem Mater* **2010**, *22*, 1173-1179.

(24) Garcia-Ruiz, A.; Morales, A.; Bokhimi, X. *J Alloy Compd* **2010**, *495*, 583-587.

(25) Kandiel, T. A.; Feldhoff, A.; Robben, L.; Dillert, R.; Bahnemann, D. W. *Chem Mater* **2010**, *22*, 2050-2060.

(26) Pan, H.; Qiu, X. F.; Ivanovc, I. N.; Meyer, H. M.; Wang, W.; Zhu, W. G.; Paranthaman, M. P.; Zhang, Z. Y.; Eres, G.; Gu, B. H. *Applied Catalysis B-Environmental* **2009**, *93*, 90-95.

(27) Di Paola, A.; Bellardita, M.; Ceccato, R.; Palmisano, L.; Parrino, F. *Journal of Physical Chemistry C* **2009**, *113*, 15166-15174.

(28) Yu, J. C.; Zhang, L. Z.; Yu, J. G. *Chem Mater* **2002**, *14*, 4647-4653.

(29) Ardizzone, S.; Bianchi, C. L.; Cappelletti, G.; Gialanella, S.; Pirola, C.; Ragaini, V. *Journal of Physical Chemistry C* **2007**, *111*, 13222-13231.

(30) Bakardjieva, S.; Subrt, J.; Stengl, V.; Dianez, M. J.; Sayagues, M. J. *Applied Catalysis B-Environmental* **2005**, *58*, 193-202.

(31) Boehme, M.; Ensinger, W. *Nano-Micro Lett.* **2011**, *3*, 236-241.

(32) Li, J.; Xu, D. *Chem Commun* **2010**, *46*, 2301-2303.

(33) Ye, L.; Mao, J.; Peng, T.; Zan, L.; Zhang, Y. *Phys. Chem. Chem. Phys.* **2014**, *16*, 15675-15680.

(34) Pan, J.; Liu, G.; Lu, G. Q. M.; Cheng, H. M. *Angew. Chem. Int. Ed. Engl.* **2011**, *50*, 2133-2137.

(35) Pan, J.; Wu, X.; Wang, L. Z.; Liu, G.; Lu, G. Q.; Cheng, H. M. *Chem Commun* **2011**, *47*, 8361-8363.

(36) Zhao, X.; Jin, W.; Cai, J.; Ye, J.; Li, Z.; Ma, Y.; Xie, J.; Qi, L. *Adv. Funct. Mater.* **2011**, *21*, 3554-3563.

(37) Liu, L. J.; Jiang, Y. Q.; Zhao, H. L.; Chen, J. T.; Cheng, J. L.; Yang, K. S.; Li, Y. *ACS Catal.* **2016**, *6*, 1097-1108.

(38) Calatayud, M.; Minot, C. *Surf. Sci.* **2004**, *552*, 169-179.

(39) Beltran, A.; Sambrano, J.; Calatayud, M.; Sensato, F.; Andres, J. *Surf. Sci.* **2001**, *490*, 116-124.

(40) Wu, B.; Guo, C.; Zheng, N.; Xie, Z.; Stucky, G. D. *J. Am. Chem. Soc.* **2008**, *130*, 17563-17567.

(41) Bermudez, V. *J. Phys. Chem. C* **2011**, *115*, 6741-6747.

(42) Tan, S.; Zhao, Y.; Zhao, J.; Wang, Z.; Ma, C.; Zhao, A.; Wang, B.; Luo, Y.; Yang, J.; Hou, J. *Phys. Rev. B* **2011**, *84*, 155418.

(43) Lee, J.; Sorescu, D. C.; Deng, X. *J. Am. Chem. Soc.* **2011**, *133*, 10066-10069.

(44) Pipornpong, W.; Wanbayor, R.; Ruangpornvisuti, V. *Appl Surf Sci* **2011**, *257*, 10322-10328.

(45) Thompson, T. L.; Yates, J. T., Jr. *Chem. Rev.* **2006**, *106*, 4428-4453.

(46) Liu, L.; Zhao, C.; Li, Y. *J. Phys. Chem. C* **2012**, *116*, 7904-7912.

(47) Pacchioni, G. *Chemphyschem* **2003**, *4*, 1041-1047.

(48) Portillo-Vélez, N.; Olvera-Neria, O.; Hernández-Pérez, I.; Rubio-Ponce, A. *Surf. Sci.* **2013**, *616*, 115-119.

(49) Li, T. C.; Goes, M. S.; Fabregat-Santiago, F.; Bisquert, J.; Bueno, P. R.; Prasittichai, C.; Hupp, J. T.; Marks, T. J. *J. Phys. Chem. C* **2009**, *113*, 18385-18390.

(50) Le Formal, F.; Tetreault, N.; Cornuz, M.; Moehl, T.; Gratzel, M.; Sivula, K. *Chem Sci* **2011**, *2*, 737-743.

(51) Hoex, B.; Gielis, J.; Van de Sanden, M.; Kessels, W. *J. Appl. Phys.* **2008**, *104*, 113703.

(52) Kessels, W.; van Delft, J.; Dingemans, G.; Mandoc, M. In *Workshop*.

(53) Chen, M. J.; Shih, Y. T.; Wu, M. K.; Tsai, F. Y. *J. Appl. Phys.* **2007**, *101*.

(54) Profijt, H.; Potts, S.; Van de Sanden, M.; Kessels, W. *J. Vac. Sci. Technol., A* **2011**, *29*, 050801.

(55) Xie, S.; Wang, Y.; Zhang, Q.; Fan, W.; Deng, W.; Wang, Y. *Chemical Communications* **2013**, *49*, 2451-2453.

(56) Liu, L.; Zhao, C.; Zhao, H.; Pitts, D.; Li, Y. *Chemical Communications* **2013**, *49*, 3664-3666.

(57) Liu, L.; Zhao, C.; Pitts, D.; Zhao, H.; Li, Y. *Catalysis Science Technology* **2014**, *4*, 1539-1546.

(58) Ahmed, N.; Shibata, Y.; Taniguchi, T.; Izumi, Y. *Journal of Catalysis* **2011**, *279*, 123-135.

(59) Yong, Z.; Rodrigues, A. E. *Energ Convers Manage* **2002**, *43*, 1865-1876.

(60) Yong, Z.; Mata, V.; Rodriguez, A. E. *Ind Eng Chem Res* **2001**, *40*, 204-209.

(61) Ram Reddy, M. K.; Xu, Z. P.; Lu, G. Q.; Diniz da Costa, J. C. *Ind Eng Chem Res* **2006**, *45*, 7504-7509.

(62) Lu, R. J.; Xu, X.; Chang, J. P.; Zhu, Y.; Xu, S. L.; Zhang, F. Z. *Applied Catalysis B-Environmental* **2012**, *111*, 389-396.

(63) Liu, L. J.; Zhao, C. Y.; Xu, J. Y.; Li, Y. *Applied Catalysis B-Environmental* **2015**, *179*, 489-499.

(64) Hong, J.; Zhang, W.; Wang, Y.; Zhou, T.; Xu, R. *ChemCatChem* **2014**, *6*, 2315-2321.

(65) Kawahara, T.; Konishi, Y.; Tada, H.; Tohge, N.; Nishii, J.; Ito, S. *Angewandte Chemie-International Edition* **2002**, *41*, 2811-2813.

(66) Carneiro, J. T.; Savenije, T. J.; Moulijn, J. A.; Mul, G. *J. Phys. Chem. C* **2011**, *115*, 2211-2217.

(67) Liu, G.; Yan, X. X.; Chen, Z. G.; Wang, X. W.; Wang, L. Z.; Lu, G. Q.; Cheng, H. M. *Journal of Materials Chemistry* **2009**, *19*, 6590-6596.

(68) Li, G. H.; Richter, C. P.; Milot, R. L.; Cai, L.; Schmuttenmaer, C. A.; Crabtree, R. H.; Brudvig, G. W.; Batista, V. S. *Dalton Trans.* **2009**, 10078-10085.

(69) Hurum, D. C.; Agrios, A. G.; Gray, K. A.; Rajh, T.; Thurnauer, M. C. *J. Phys. Chem. B* **2003**, *107*, 4545-4549.

(70) Ohtani, B.; Prieto-Mahaney, O. O.; Li, D.; Abe, R. *J Photoch Photobio A* **2010**, *216*, 179-182.

(71) Bahnemann, D. W.; Kandiel, T. A.; Feldhoff, A.; Robben, L.; Dillert, R. *Chem Mater* **2010**, *22*, 2050-2060.

(72) Wenk, H. R.; Lutterotti, L.; Vogel, S. C. *Powder Diffr.* **2010**, *25*, 283-296.

(73) Rezaee, M.; Khoie, S. M. M.; Liu, K. H. *Crystengcomm* **2011**, *13*, 5055-5061.

(74) Gong, X. Q.; Selloni, A. *Physical Review B* **2007**, *76*, 11.

(75) Moonoosawmy, K. R.; Katzke, H.; Es-Souni, M.; Dietze, M.; Es-Souni, M. *Langmuir* **2012**, *28*, 6706-6713.

(76) Nagaveni, K.; Hegde, M. S.; Ravishankar, N.; Subbanna, G. N.; Madras, G. *Langmuir* **2004**, *20*, 2900-2907.

(77) Kandiel, T. A.; Robben, L.; Alkaim, A.; Bahnemann, D. *Photochemical & Photobiological Sciences* **2013**, *12*, 602-609.

(78) Varghese, O. K.; Paulose, M.; LaTempa, T. J.; Grimes, C. A. *Nano Lett.* **2009**, *9*, 731-737.

(79) Chen, X. B.; Liu, L.; Yu, P. Y.; Mao, S. S. *Science* **2011**, *331*, 746-750.

(80) Pan, H.; Gu, B. H.; Zhang, Z. Y. *J. Chem. Theory Comput.* **2009**, *5*, 3074-3078.

(81) Wohlgemuth, S. A.; White, R. J.; Willinger, M. G.; Titirici, M. M.; Antonietti, M. *Green Chem* **2012**, *14*, 1515-1523.

(82) Wang, W.-N.; An, W.-J.; Ramalingam, B.; Mukherjee, S.; Niedzwiedzki, D. M.; Gangopadhyay, S.; Biswas, P. *J Am Chem Soc* **2012**, *134*, 11276-11281.

(83) Su, W.; Zhang, J.; Feng, Z.; Chen, T.; Ying, P.; Li, C. *The Journal of Physical Chemistry C* **2008**, *112*, 7710-7716.

(84) Yang, C.-C.; Yu, Y.-H.; van der Linden, B.; Wu, J. C. S.; Mul, G. *J Am Chem Soc* **2010**, *132*, 8398-8406.

(85) Liu, L. J.; Zhao, C. Y.; Li, Y. *Journal of Physical Chemistry C* **2012**, *116*, 7904-7912.

(86) Liu, L. J.; Li, Y. *Aerosol Air Qual Res* **2014**, *14*, 453-469.

(87) Gomes Silva, C.; Bouizi, Y.; Fornes, V.; Garcia, H. *J Am Chem Soc* **2009**, *131*, 13833-13839.

(88) Parida, K.; Satpathy, M.; Mohapatra, L. *Journal of Materials Chemistry* **2012**, *22*, 7350.

(89) Zhao, Y.; Chen, P.; Zhang, B.; Su, D. S.; Zhang, S.; Tian, L.; Lu, J.; Li, Z.; Cao, X.; Wang, B.; Wei, M.; Evans, D. G.; Duan, X. *Chemistry* **2012**, *18*, 11949-11958.

(90) Yanagisawa, K.; Ovenstone, J. *J Phys Chem B* **1999**, *103*, 7781-7787.

(91) Assaker, K.; Carteret, C.; Lebeau, B.; Marichal, C.; Vidal, L.; Stébé, M.-J.; Blin, J.-L. *ACS Sustainable Chemistry & Engineering* **2013**, *2*, 120-125.

(92) Chen, W.; Qu, B. J. *Chem Mater* **2003**, *15*, 3208-3213.

(93) Ardanuy, M.; Velasco, J. I. *Appl Clay Sci* **2011**, *51*, 341-347.

(94) Rives, V. *Layered double hydroxides: present and future*; Nova Publishers, 2001.

(95) Millange, F.; Walton, R. I.; O'Hare, D. *Journal of Materials Chemistry* **2000**, *10*, 1713-1720.

(96) Leon, M.; Diaz, E.; Bennici, S.; Vega, A.; Ordonez, S.; Auroux, A. *Ind Eng Chem Res* **2010**, *49*, 3663-3671.

(97) Sharma, U.; Tyagi, B.; Jasra, R. V. *Ind Eng Chem Res* **2008**, *47*, 9588-9595.

(98) Yanagisawa, K.; Yamamoto, Y.; Feng, Q.; Yamasaki, N. *J Mater Res* **1998**, *13*, 825-829.

(99) Wang, Y. C.; Zhang, F. Z.; Xu, S. L.; Yang, L.; Li, D. Q.; Evans, D. G.; Duan, X. *Chem Eng Sci* **2008**, *63*, 4306-4312.

(100) Yoo, J. S.; Bhattacharyya, A. A.; Radlowski, C. A. *Ind Eng Chem Res* **1991**, *30*, 1444-1448.

(101) Kanezaki, E. *Solid State Ionics* **1998**, *106*, 279-284.

(102) Myerson, A. *Handbook of industrial crystallization*; Butterworth-Heinemann, 2002.

(103) Xu, Z. P.; Stevenson, G.; Lu, C.-Q.; Lu, G. Q. *The Journal of Physical Chemistry B* **2006**, *110*, 16923-16929.

(104) He, J.; Wei, M.; Li, B.; Kang, Y.; Evans, D. G.; Duan, X. In *Layered double hydroxides*; Springer: 2006, p 89-119.

(105) Shimamura, A.; Perander, L.; Kanezaki, E.; Jones, M. I.; Metson, J. B. In *Materials Science Forum*; Trans Tech Publications: 2012; Vol. 700, p 67-70.

(106) Wang, Q.; Gao, Y. S.; Luo, J. Z.; Zhong, Z. Y.; Borgna, A.; Guo, Z. H.; O'Hare, D. *Rsc Adv* **2013**, *3*, 3414-3420.

(107) Zeng, S. B.; Xu, X. L.; Wang, S. K.; Gong, Q. K.; Liu, R. J.; Yu, Y. *Mater Chem Phys* **2013**, *140*, 159-167.

(108) Zhu, H. X.; Liu, J. M. *Comp Mater Sci* **2014**, *85*, 164-171.

(109) Li, Y.; Wang, W.-N.; Zhan, Z.; Woo, M.-H.; Wu, C.-Y.; Biswas, P. *Applied Catalysis B: Environmental* **2010**, *100*, 386-392.

(110) Koci, K.; Obalova, L.; Matejova, L.; Placha, D.; Lacny, Z.; Jirkovsky, J.; Solcova, O. *Applied Catalysis B-Environmental* **2009**, *89*, 494-502.

(111) Almquist, C. B.; Biswas, P. *Journal of Catalysis* **2002**, *212*, 145-156.

(112) Yang, H. G.; Sun, C. H.; Qiao, S. Z.; Zou, J.; Liu, G.; Smith, S. C.; Cheng, H. M.; Lu, G. Q. *Nature* **2008**, *453*, 638-641.

(113) Zhao, H. L.; Liu, L. J.; Andino, J. M.; Li, Y. *J. Mater. Chem. A* **2013**, *1*, 8209-8216.

(114) Ameta, S.; Ameta, R. *Solar Energy Conversion and Storage: Photochemical Modes*; CRC Press, 2015; Vol. 10.

(115) Slamet, H.; Purnama, E.; Riyani, K.; Gunlazuardi, J. *World Applied Sciences Journal* **2009**, *6*, 112-122.

(116) Slamet, H.; Nasution, H.; Purnama, E.; Kosela, S.; Gunlazuardi, J. *Catal. Commun.* **2005**, *6*, 313-319.

(117) Wei, Y.; Liu, H.; Sheng, O.; Liu, Z.; Chen, S.; Yang, L. *Appl. Opt.* **2011**, *50*, 4720-4727.

(118) Pan, F.; Wu, K.; Li, H. X.; Xu, G. Q.; Chen, W. *Chem-Eur J* **2014**, *20*, 15095-15101.

(119) Nguyen, C. K.; Cha, H. G.; Kang, Y. S. *Cryst. Growth Des.* **2011**, *11*, 3947-3953.

(120) Tan, H.; Zhao, Z.; Zhu, W.; Coker, E.; Li, B.; Zheng, M.; Yu, W.; Fan, H.; Sun, Z. *Acs Appl Mater Inter* **2014**, *6*, 19184-19190.

(121) Lin, Y.; Yang, Y.; Zhuang, B.; Huang, S.; Wu, L.; Huang, Z.; Zhang, F.; Du, Y. *Journal of Physics D: Applied Physics* **2008**, *41*, 195007.

(122) Rath, C.; Mohanty, P.; Pandey, A.; Mishra, N. *Journal of Physics D: Applied Physics* **2009**, *42*, 205101.

(123) Liu, Y.; Zhang, B.; Luo, L.; Chen, X.; Wang, Z.; Wu, E.; Su, D.; Huang, W. *Angewandte Chemie International Edition* **2015**, *54*, 15260-15265.

(124) Lin, Y.-T.; Zeng, T.-W.; Lai, W.-Z.; Chen, C.-W.; Lin, Y.-Y.; Chang, Y.-S.; Su, W.-F. *Nanotechnology* **2006**, *17*, 5781.

(125) Nowotny, J.; Bak, T.; Nowotny, M.; Sheppard, L. *J. Phys. Chem. B* **2006**, *110*, 18492-18495.

(126) Hoex, B.; Schmidt, J.; Pohl, P.; Van de Sanden, M.; Kessels, W. *Journal of Applied Physics* **2008**, *104*, 044903.

(127) Schmidt, J.; Veith, B.; Brendel, R. *physica status solidi (RRL)-Rapid Research Letters* **2009**, *3*, 287-289.

(128) Richter, A.; Benick, J.; Hermle, M.; Glunz, S. W. *physica status solidi (RRL)-Rapid Research Letters* **2011**, *5*, 202-204.

(129) Zhao, Z.; Zhang, X. H.; Zhang, G.; Liu, Z.; Qu, D.; Miao, X.; Feng, P.; Sun, Z. *Nano Res.* **2015**, *8*, 4061-4071.

(130) Yan, J.; Wu, G.; Guan, N.; Li, L.; Li, Z.; Cao, X. *Phys. Chem. Chem. Phys.* **2013**, *15*, 10978-10988.